

AperTO - Archivio Istituzionale Open Access dell'Università di Torino

Petrology of blueschist from the Western Himalaya (Ladakh, NW India): Exploring the complex behavior of a lawsonite-bearing system in a paleo-accretionary setting

This is the author's manuscript

Original Citation:

Availability:

This version is available <http://hdl.handle.net/2318/1565724> since 2021-04-19T12:47:09Z

Published version:

DOI:10.1016/j.lithos.2016.02.014

Terms of use:

Open Access

Anyone can freely access the full text of works made available as "Open Access". Works made available under a Creative Commons license can be used according to the terms and conditions of said license. Use of all other works requires consent of the right holder (author or publisher) if not exempted from copyright protection by the applicable law.

(Article begins on next page)

**PETROLOGY OF BLUESCHIST FROM THE WESTERN HIMALAYA (LADAKH, NW INDIA):
EXPLORING THE COMPLEX BEHAVIOUR OF A LAWSONITE-BEARING SYSTEM IN A
PALAEO-ACCRETIONARY SETTING**

Chiara Groppo^{a,b}, Franco Rolfo^{a,b}, Himanshu K. Sachan^c, Santosh K. Rai^c

a - Department of Earth Sciences, University of Torino, Via Valperga Caluso 35, Torino, 10125, Italy

b - IGG-CNR, Via Valperga Caluso 35, Torino, 10125, Italy

c - Wadia Institute of Himalayan Geology, Dehra Dun, 248001, India

Corresponding Author

Chiara Groppo

Dept. of Earth Sciences, University of Torino

Via Valperga Caluso, 35 – 10125 Torino, Italy

Tel. +39 0116705106

Fax +39 0116705128

E-mail: chiara.groppo@unito.it

1. Introduction

Lawsonite-bearing blueschists and eclogites are witnesses of cold subduction processes occurred along ancient convergent margins. Metamorphic processes involved in the generation and preservation of lawsonite are crucial in many research areas, ranging from petrology to geochemistry, geodynamics and geophysics (e.g. Hacker et al., 2003; Bebout, 2007; Hacker, 2008; Davis, 2011; Martin et al., 2011; Vitale Brovarone et al., 2011; Chantel et al., 2012; Abers et al., 2013; Cao et al., 2013; Kim et al., 2013; Spandler & Pirard, 2013). Therefore, lawsonite-bearing eclogites and, to a lesser extent, lawsonite-bearing blueschists have been the focus of several studies, especially in recent years (Tsujimori and Ernst, 2014 and references therein). Compared to the rare occurrences of lawsonite eclogites worldwide (see the review paper by Tsujimori et al., 2006), lawsonite blueschist units are reported from several orogenic belts (e.g. Agard et al., 2009; Tsujimori and Ernst, 2014 and references therein); however, in many cases, the lawsonite blueschist-facies assemblages formed at peak metamorphic conditions are widely overprinted by epidote blueschist- and/or greenschist-facies retrograde assemblages during exhumation (e.g. Ernst, 1988; Agard et al., 2001, 2006; Jolivet et al., 2003; Schumacher et al., 2008; Plunder et al., 2012). Lawsonite preservation requires exhumation along cold geothermal gradients, comparable to those required for its formation during subduction. Such geothermal regimes are typical of ancient Pacific-type plate convergent margins (see Tsujimori and Ernst, 2014 for a review); the occurrence of well-preserved high-pressure lawsonite blueschists and eclogites in an orogenic belt is therefore an appealing clue of a peculiar tectonic setting.

Although the Himalaya is the archetype of collisional orogens, formed as a consequence of the closure of the Tethyan ocean separating India from Asia followed by continental collision between the two plates, high-pressure metamorphic rocks are rare along the orogen (e.g. Lombardo and Rolfo, 2002; Guillot et al., 2008). Moreover, most of the eclogites reported so far from the Himalaya correspond to the metamorphosed continental Indian crust dragged below Asia (NW Himalaya: Kaghan, Tso Moriri and Stak massifs; Pognante and Spencer, 1991; Guillot et al., 1997, 1999, 2007, 2008; de Sigoyer et al., 2000; O'Brien et al., 2001; Sachan et al., 2004; Lanari et al., 2013), or underthrust beneath southern Tibet (E Himalaya: Kharta and Bhutan; Lombardo and Rolfo, 2002; Groppo et al., 2007; Chakungal et al., 2010; Grujic et al., 2011; Warren et al., 2011). Evidence of the ancient Tethyan oceanic crust subducted below Asia are also rare and locally occur within the Indus-Tsangpo Suture (ITS) zone, which separates the northern margin of the Indian plate to the south (i.e. the Himalaya s.s.) from the southern margin of the Asian plate to the north (represented, from west to east, by the Kohistan Arc, the Ladakh block and the Lhasa block). These evidences are: (i) few lawsonite blueschists from the western part of the ITS zone in Pakistan (Shangla: Shams, 1972; Frank et al., 1977) and Ladakh (NW India) (Sapi-Shergol: Honegger et al., 1989; Zildat: Viridi et al., 1977; de Sigoyer et al., 2004), interpreted as related to paleo-accretionary prisms formed in response to the subduction of the Neo-Tethyan ocean below the Asian plate (e.g. Robertson, 2000; Mahéo et al., 2006; Guillot et al., 2008); (ii) few eclogite, lawsonite- and epidote blueschist -facies rocks reported from the Indo-Burmese Ranges (Nagaland Ophiolite Complex: Ghose and Singh, 1980; Acharyya, 1986; Chatterjee and Ghose, 2010; Ao and Bhowmik, 2014; Bhowmik and Ao, 2015; Chin Hill Ophiolite: Socquet et al., 2002), interpreted as the eastern extension of the ITS zone. These rare high-pressure/low-temperature (HP-LT) rocks are therefore crucial for constraining the evolution of the India-Asia convergence zone during the closure of the Neo-Tethyan ocean (Guillot et al., 2008); in this framework, the detailed reconstruction of their P-T paths is a fundamental step toward a reliable geodynamic interpretation.

The P-T evolution of the eclogites and blueschists from the Indo-Burmese Ranges has been recently constrained by means of modern petrological methods (e.g. pseudosections); variable peak P-T conditions have been reported from different portions of the suture zone, ranging from ~340 °C, ~11.5 kbar (lawsonite blueschists: Ao and Bhowmik, 2014) to 540 ± 35 °C, 14.4 ± 2 kbar (epidote blueschists: Bhowmik and Ao,

2015) to 580-610°C and 17-20 kbar (eclogites: Chatterjee and Ghose, 2010). On the opposite, modern petrologic studies aimed at constraining the P-T evolution of the blueschist-facies rocks from the western sector of the ITS zone are lacking. Some 25 years ago, Honegger et al. (1989) reported peak metamorphic conditions of 350-420 °C, 9-11 kbar for the Sapi-Shergol lawsonite blueschists using conventional thermobarometry. P-T estimates for the Shangla blueschists were published even earlier (Guiraud, 1982; Jan, 1985) and suggest peak P-T conditions of ca. 400 °C, 5 kbar. Although detailed, these petrological studies are based on conventional methods and need to be updated using more recent and powerful petrological approaches (e.g. isochemical phase diagrams).

In this paper, the lawsonite blueschists from Sapi-Shergol have been petrologically re-investigated with the aims of: (i) constraining their P-T evolution; (ii) evaluating the influence of Fe₂O₃ and of H₂O on the stability of the high pressure mineral assemblages; (iii) understanding the processes controlling lawsonite formation and preservation, and (iv) interpreting the P-T evolution of the Sapi-Shergol blueschists in the framework of India-Asia collision.

2. Geological setting

In the India–Asia convergence system, the ITS zone records the closure of the Neo-Tethyan ocean from Late Cretaceous to Tertiary time (Frank et al., 1977; Honegger et al., 1989; Cannat and Mascle, 1990). Among the few occurrences of high-pressure rocks along the ITS, those of Ladakh (NW India) are the best in terms of rock freshness, areal extent and metamorphic assemblages. Blueschists in the Ladakh area occur along the ITS in few localities: from SE to NW these are Puga, Urti, Hinju and Sapi-Shergol (Honegger et al., 1989). The largest outcrop is that of Sapi-Shergol (35 km south of Kargil), where the blueschists form a 12 km x 1 km E-W trending narrow zone.

Tectonically, the Sapi-Shergol blueschists belong to a narrow belt called “Ophiolitic Mélange Unit” (Honegger et al., 1989) (Fig. 1), which outcrops over a distance of 250 km along the ITS suture. This belt consists of several thrust slices sandwiched between the Nindam-Naktul-Dras nappes to the north, and the Lamayuru-Karamba nappes to the south. The Ophiolitic Mélange Unit is interpreted as a relic of a paleo-accretionary prism formed in response to the northward subduction of the Neo-Tethyan ocean, originally separating the Ladakh arc to the south from the southern Asian active margin to the north (Mahéo et al., 2006). This paleo-accretionary prism consists of sedimentary units including blocks of (mainly) basic lithologies that have been metamorphosed under variable P-T conditions, ranging from low-grade metamorphism to lawsonite blueschist -facies metamorphism (Frank et al., 1977; Honegger et al., 1989; Jan, 1987; Reuber et al., 1987; Sutra, 1990; Ahmad et al., 1996; Robertson, 2000; Mahéo et al., 2006).

The Sapi-Shergol Ophiolitic Mélange (SSOM) is a complex unit which includes slices of the paleo-accretionary prism, intercalated with numerous slices of other units including the Nindam and Lamayuru turbidites and low grade meta-ophiolitic slices consisting of serpentinized peridotites intruded by basic dikes (“sheared serpentinites” of Robertson, 2000). The narrow blueschist zone cropping out close to the village of Sher gol (Fig. 1, 2a) is overlain discordantly by the Sher gol conglomerate of post-Eocene (Oligo-Miocene?) age (Honegger et al., 1989). Blueschist lithologies are dominated by volcanoclastic sequences of basic material (Fig. 2b,c) with subordinate interbedding of cherts and minor carbonatic lithologies. Mahéo et al. (2006) suggested that the blueschists derive from calc-alkaline igneous rocks formed in an intra-oceanic arc environment. K-Ar ages of whole-rocks and glaucophane suggest an age of ca. 100 Ma for the high-pressure metamorphism (Honegger et al., 1989).

2.1 Main blueschist lithologies of the SSOM

113 Metabasic and metavolcanoclastic rocks are the dominant lithologies in the SSOM, and they are associated
114 to subordinate interbedded metasediments. These lithologies have been described in detail by Honegger et
115 al. (1989); the most relevant petrographic features are therefore only summarized here.

116

117 *2.1.1 Metabasic and metavolcanoclastic rocks*

118 Metabasic rocks are mainly represented by fine-grained glaucophane-bearing schists (Fig. 2c,e) with
119 variable amounts of lawsonite and minor clinopyroxene and phengite. Lawsonite can be either fine-grained
120 or porphyroblastic and it generally overgrows the main foliation defined by the alignment of glaucophane ±
121 phengite (Fig. 2e); where present, phengite often shows a slightly greenish pleochroism. Clinopyroxene
122 (omphacite/aegirine-augite) generally occurs as fine-grained dusty and fibrous aggregates, probably
123 replacing former magmatic clinopyroxene fenocrysts. Fine-grained titanite aggregates are often aligned to
124 the main foliation (Fig. 2e); opaque minerals can be locally abundant and surrounded by pressure fringes of
125 albite. Locally, remnants of a strongly vesiculated structure are evidenced by the alignment of fine-grained
126 titanite.

127 Metavolcanoclastic rocks are characterized by a clastic structure and consist of irregular fragments of
128 metabasic rocks set in a very fine-grained matrix (Fig. 2b). Clasts of metabasic rocks are either rounded or
129 sharp and vary in size from few millimeters to several centimeters (Fig. 2b, d). The clasts generally consist
130 of blue amphibole + lawsonite ± minor clinopyroxene in different modal abundances and with different
131 grain-size (Fig. 2d). The matrix is generally very fine-grained and mainly consists of blue amphibole, green
132 clinopyroxene (aegirine/omphacite) forming fine-grained dusty aggregates, porphyroblastic lawsonite and
133 minor phengite and chlorite. Fine-grained aggregates of titanite (leucoxene) replace former ilmenite.

134 Both metabasic rocks and metavolcanoclastic rocks can be crosscut by glaucophane veins and/or late albite
135 ± calcite, and albite + chlorite ± quartz veins.

136

137 *2.1.2 Metasediments*

138 Both silicic and impure carbonatic metasediments occur as intercalations in the metabasic and
139 metavolcanoclastic rocks. Among the silicic metasediments, glaucophane + lawsonite + phengite ± garnet
140 schists, lawsonite + glaucophane + phengite + garnet quartzitic-micaschists and glaucophane + garnet +
141 phengite quartzites (Fig. 2f) are the most common types. Lawsonite and garnet can be either fine-grained
142 or porphyroblastic. Lawsonite and garnet porphyroblasts can reach few centimeters and few millimeters in
143 size, respectively, and generally overgrow the main foliation; lawsonite porphyroblasts are locally dusty due
144 to the presence of abundant fluid inclusions. Glaucophane and phengite are always fine-grained and define
145 the main foliation, which is often intensely crenulated. Titanite is ubiquitous as accessory mineral. The
146 lawsonite blueschists investigated in detail in this paper belong to this group of metasediments.

147 The impure carbonatic metasediments are very fine-grained and mainly consist of lawsonite, calcite,
148 glaucophane and minor phengite ± prehnite (Fig. 2g). Calcite often occurs as large poikiloblasts including
149 idioblastic lawsonite. Prehnite is rare and occurs as reniform globular aggregates of fine-grained brownish
150 fibrous crystals.

151 Late quartz, albite ± quartz and calcite ± albite veins crosscut the main schistosity in most metasediments.

152

153 **3. Methods**

154 *3.1 Micro-X-ray fluorescence (μ-XRF) maps*

155 The micro-XRF maps of the whole thin sections (Fig. 3 and Fig. SM1, SM2) were acquired using a μ-XRF
156 Eagle III-XPL spectrometer equipped with an EDS Si(Li) detector and with an Edax Vision32 microanalytical
157 system (Department of Earth Sciences, University of Torino, Italy). The operating conditions were as

follows: 100 ms counting time, 40 kV accelerating voltage and a probe current of 900 μ A. A spatial resolution of about 65 μ m in both x and y directions was used. Quantitative modal percentages of each mineral were obtained by processing the μ -XRF maps with the software program “Petromod” (Cossio et al. 2002).

3.2 Mineral chemistry

Minerals were analysed with a Cambridge Stereoscan 360 SEM equipped with an EDS Energy 200 and a Pentafet detector (Oxford Instruments) at the Department of Earth Sciences, University of Torino. The operating conditions were as follows: 50 s counting time and 15 kV accelerating voltage. SEM–EDS quantitative data (spot size = 2 μ m) were acquired and processed using the Microanalysis Suite Issue 12, INCA Suite version 4.01; natural mineral standards were used to calibrate the raw data; the $\rho\rho Z$ correction (Pouchou and Pichoir, 1988) was applied. Absolute error is 1 σ for all calculated oxides.

Mineral chemical data of representative minerals are reported in Tables SM1, SM2. Structural formulae have been calculated on the basis of 12 oxygens for garnet, 6 oxygens for omphacite, 8 oxygens for lawsonite, 11 oxygens for phengite and 23 oxygens for amphibole. Fe^{+3} has been calculated by stoichiometry except for amphibole (average Fe^{+3} values).

3.3 Phase diagrams computation

Isochemical phase diagrams were calculated in the MnNCKFMASH(O) system using Perple_X (version 6.7.1, Connolly 1990, 2009) and the thermodynamic dataset and equation of state for H_2O – CO_2 fluid of Holland and Powell (1998, revised 2004). The following solid solution models were used: garnet (Holland and Powell, 1998), amphibole (Diener et al., 2007, 2012), omphacite (Green et al., 2007; Diener et al., 2012), chlorite (Holland et al., 1998), phengite (Holland and Powell, 1998), plagioclase (Newton et al., 1980) and epidote (Holland and Powell, 1998). Quartz, lawsonite, and zoisite were considered as pure end-members. The bulk rock compositions of the studied samples have been calculated by combining the mineral proportions obtained from the modal estimate of micro-XRF maps (Fig. 3, Table 1) with mineral chemistry acquired at SEM–EDS, and are reported in Table 1: these whole rock compositions have been used to model: (i) the whole prograde P–T evolution in sample 14-4B; (ii) the growth of garnet core + mantle in sample 14-6F. For this last sample, the possible effects of chemical fractionation of the bulk composition due to the growth of the strongly zoned garnet porphyroblasts have been also considered. The bulk composition effectively in equilibrium during the growth of garnet rim has been therefore calculated by subtracting the garnet core and mantle compositions (i.e. the modal amount of garnet core + mantle was estimated from the micro-XRF maps as 3.5 vol%) to the whole rock composition (Table 1).

4. Petrography and mineral chemistry

Among the various lithologies observed in the study area, two metasediments (samples 14-4B and 14-6F/G) have been petrologically investigated in detail; they are both characterized by a relatively simple and very well preserved mineral assemblage, but differ for the grain size and the modal abundance of each phase (Table 1). Samples 14-6F/G derive from the same hand specimen (two different thin sections cut parallel and perpendicular to the main lineation); petrography and mineral chemistry refer to both thin sections, whereas the micro-XRF map and the thermodynamic modeling refer to sample 14-6F only.

4.1 Sample 14-4B

Sample 14-4B is a fine-grained lawsonite + glaucophane + garnet -bearing quartzitic-micaschist characterized by mm-thick quartz-rich layers alternating with mm-thick lawsonite + phengite-rich layers

(Fig. 4a). The main foliation, defined by the preferred orientation of phengite and glaucophane in both domains, is crosscut by late quartz-bearing and calcite \pm albite -bearing veins (Fig. 3, and Fig. SM1). Microstructural relationships between quartz (42 vol%), lawsonite (21 vol%), phengite (22 vol%), glaucophane (12 vol%) and garnet (3 vol%) suggest that these minerals all belong to the equilibrium assemblage (Fig. 7). Abundant titanite and minor pyrite occur as accessory minerals. Lawsonite occurs as fine-grained idiomorphs (Fig. 4) with quartz \pm titanite inclusions; in the quartz-rich layers, lawsonite is often crowded of quartz inclusions, locally assuming a skeletal habit. It is almost pure in composition, with a very low Fe content (0.00-0.30 a.p.f.u. on the basis of 8 oxygens). The fine-grained phengite (Fig. 4b,c) shows a relatively large compositional spread in Si, Al_{tot} and (Mg + Fe_{tot}). Its Si content ranges between 3.53 and 3.81 a.p.f.u. (on the basis of 11 oxygens), with the most frequent values in the range 3.53-3.64 a.p.f.u (Fig. 6d). Most of the phengite compositions broadly lie along the celadonite-muscovite compositional joint, reflecting the dominant role of Tschermak's substitution; phengite with the lowest Si contents, however, plot slightly away from the celadonite- muscovite joint in both Si vs. Al_{tot} and (Mg + Fe_{tot}) vs. Si diagrams, thus suggesting the existence of very low Fe⁺³ contents (Vidal and Parra, 2000). Blue amphibole occurs as fine-grained idiomorphs associated to phengite and lawsonite (Fig. 4a,b), and it is slightly zoned, with a lighter blue core and a darker blue rim. Both cores and rims are ferroglaucofane according to the classification of Leake et al. (1997), but are characterized by slightly different Si (on the basis of 23 oxygens), XNa (XNa=Na/(Na+Ca)) and XFe⁺³ (XFe⁺³=Fe⁺³/Fe_{tot}) contents (core: Si = 7.62-7.74 a.p.f.u., XNa=0.92-0.95, XFe⁺³=0.23-0.27; rim: Si = 7.91-7.97 a.p.f.u., XNa=0.98-1.00, XFe⁺³=0.10-0.21) (Fig. 6e,f). Garnet occurs as small slightly zoned idiomorphs (up to 0.3 mm in diameter) (Fig. 4a), particularly enriched in Mn (Fig. 6a). XSp decreases and XAlm and XPrp increase from core to rim, whereas XGrs is almost homogeneous (core: Sps₅₅₋₆₀Alm₂₀₋₂₅Grs₁₅₋₂₂Prp_{0-0.6}; mantle: Sps₅₀₋₅₄Alm₂₅₋₂₈Grs₁₆₋₂₃Prp_{0.4-0.9}; rim: Sps₄₄₋₄₇Alm₃₀₋₃₄Grs₁₈₋₂₃Prp_{0.6-1.3}) (Fig. 6a).

4.2 Sample 14-6F/G

Sample 14-6F/G is a lawsonite + glaucophane + phengite + garnet schist, dominated by glaucophane (44 vol%) + lawsonite (22 vol%) + phengite (9 vol%) + garnet (4 vol%) layers alternating with discontinuous quartz (21 vol%) -rich domains. The main foliation, defined by the preferred orientation of glaucophane and minor phengite, is overgrown by large lawsonite and garnet porphyroblasts and it is intensely crenulated (Fig. 5a,b). Lawsonite and garnet porphyroblasts crystallization occurred prior to the crenulation event (Fig. 7). Titanite occurs as accessory mineral aligned to the main foliation. Late quartz \pm albite \pm chlorite veins crosscut the main foliation (Fig. 5d, e). The fine-grained blue amphibole nematoblasts in the matrix (Fig. 5a-c) are quite homogeneous in composition; they are glaucophane according to the classification of Leake et al. (1997) and have Si = 7.71-7.99 a.p.f.u., XNa=0.85-1.00 and XFe⁺³=0.14-0.24, with Si and XNa decreasing and XFe⁺³ increasing toward the rim (Fig. 6e,f). Lawsonite occurs as large porphyroblasts, up to few centimeter in size, overgrowing the main foliation (Fig. 3, 5a-d and Fig. SM2). Lawsonite porphyroblasts are often boudinaged; the boudinage still occurred in the lawsonite stability field because lawsonite + quartz + glaucophane are also found in the pressure shadows (Fig. 5c). The Fe content in lawsonite is very low (Fe = 0.03-0.05 a.p.f.u. on the basis of 8 oxygens). Garnet porphyroblasts, up to 2-3 mm in diameter, overgrow the main foliation and are also included in lawsonite (Fig. 5). They are strongly zoned (Fig. 5e, 6a, 6b), with spessartine decreasing and almandine and pyrope increasing from core to rim (core: Sps₅₀₋₅₅Alm₁₆₋₂₁Grs₂₆₋₂₈Prp_{1.1-1.4}; mantle: Sps₄₀₋₄₈Alm₂₂₋₂₇Grs₂₉₋₃₁Prp_{1.5-1.8}; rim: Sps₂₄₋₃₀Alm₃₇₋₄₂Grs₂₇₋₃₂Prp_{2.5-3.4}) (Fig. 6a). Garnet porphyroblasts include glaucophane,

actinolite, quartz and chlorite in the core and mantle domains, and few omphacite ($\text{Jd}_{16-33}\text{Acm}_{9-17}$) (Fig. 6c), phengite ($\text{Si} = 3.80$ a.p.f.u.) and quartz in the mantle and rim domains (Fig. 5e, 5f, 6d).

Phengite occurs as small flakes in equilibrium with glaucophane (Fig. 5, 7); it is locally zoned, with the highest Si content in the rim (core: $\text{Si} = 3.36\text{--}3.57$ a.p.f.u.; rim: $\text{Si} = 3.61\text{--}3.84$ a.p.f.u. on the basis of 11 oxygens). The Fe^{+3} content in phengite is low since most of the phengite compositions lie along the celadonite-muscovite compositional joint (Fig. 6d).

5. Phase equilibria and P-T evolution

5.1 P-T pseudosection in the MnNKCFMASH system

The thermodynamic modeling approach was used to constrain the P-T evolution of the two blueschist samples. P-T pseudosections have been first calculated in the MnNKCFMASH model system ($\text{MnO-Na}_2\text{O-K}_2\text{O-CaO-FeO-MgO-Al}_2\text{O}_3\text{-SiO}_2\text{-H}_2\text{O}$), and two assumptions were made: (1) H_2O was considered in excess; (2) Fe^{+3} was not included in the calculation. The influence of these two important components on the stability of mineral assemblages will be discussed later. Concerning sample 14-6F, the fractionation effects on its bulk composition due to the growth of large garnet porphyroblasts have been considered, and two different pseudosections have been calculated: (i) a first pseudosection, calculated using the whole rock composition, has been used to model the growth of garnet core + mantle; (ii) a second pseudosection, calculated using the effective bulk composition derived by subtracting garnet cores and mantles to the whole rock composition (Table 1), has been used to model the growth of garnet rim. Fractionation effects on the bulk composition are negligible for sample 14-4B, because garnet is very small.

5.1.1 P-T evolution constrained for sample 14-4B

The topology of the pseudosection calculated for sample 14-4B is very simple and dominated by three- and four-variant fields (Fig. 8a). The observed peak assemblage Grt + Gln + Lws + Phe is modelled by a relatively narrow five-variant field at $P > 19$ kbar, which separates a chlorite-bearing field (at lower T) from an omphacite-bearing field (at higher T). At $P < 19$ kbar, both chlorite and omphacite coexist in the three-variant Grt + Gln + Lws + Phe + Chl + Omp field.

The modeled garnet compositional isopleths (core: $X_{\text{SpS}} = 0.60$, $X_{\text{Alm}} = 0.24$, $X_{\text{Grs}} = 0.15$, $X_{\text{Prp}} = 0.006$; mantle: $X_{\text{SpS}} = 0.52$, $X_{\text{Alm}} = 0.28$, $X_{\text{Grs}} = 0.18$, $X_{\text{Prp}} = 0.009$; rim: $X_{\text{SpS}} = 0.44$, $X_{\text{Alm}} = 0.30$, $X_{\text{Grs}} = 0.23$, $X_{\text{Prp}} = 0.013$) constrain the growth of garnet core, mantle and rim at about 365°C , 19.5 kbar (in the Grt + Gln + Lws + Phe + Chl field), 390°C , 20.5 kbar (in the Grt + Gln + Lws + Phe field) and 420°C , 22 kbar (in the Grt + Gln + Lws + Phe + Omp field) (Fig. 8a and Fig. SM3). The modeled modal amounts of chlorite and omphacite in equilibrium with garnet core and rim, respectively, are lower than 0.5 vol%. The modeled phengite compositional isopleths ($\text{Si} = 3.80\text{--}3.82$ a.p.f.u.) constrain the growth of phengite at P-T conditions compatible with the growth of garnet core and mantle.

The resulting prograde P-T evolution of sample 14-4B is therefore characterized by an increase in both P and T, up to peak conditions of about 420°C , 22 kbar (Fig. 8a). The modeled isomodes of the main mineral phases are consistent with the prograde growth (i.e. increase in its modal amount) of garnet along this P-T path, but predict the (slight) consumption of lawsonite (Fig. 8b; the P-T path crosses the Lws-isomodes downward), opposite to microstructural observations which suggest that garnet and lawsonite grew almost simultaneously (Fig. 7). This apparent discrepancy between the results of the thermodynamic modeling and the observed microstructure will be discussed in the following. The modeled H_2O isomodes show that during the inferred prograde evolution, a moderate de-hydration occurred, thus implying that mineral assemblages were H_2O saturated (Guiraud et al., 2001).

294 5.1.2 P-T evolution constrained for sample 14-6F

295 The topologies of the two pseudosections calculated for sample 14-6F using the whole rock composition
296 and the fractionated bulk composition are simple and dominated by three- and four-variant fields. Because
297 the two pseudosections are quite similar (the main difference is the shift of the Grt-bearing fields toward
298 higher temperatures in the fractionated pseudosection), they have been condensed in the same figure (Fig.
299 9a). Two large three-variant fields, separated by a narrow di-variant field, dominate the two
300 pseudosections: at higher P (and lower T) is stable the Chl + Grt + Act + Gln + Lws + Phe assemblage,
301 whereas at lower P (and higher T) is stable the Chl + Grt + Gln + Lws + Omp + Phe assemblage.

302 The modeled garnet compositional isopleths from the unfractionated pseudosection (core: $X_{\text{Sps}}=0.55$,
303 $X_{\text{Alm}}=0.18$, $X_{\text{Grs}}=0.27$, $X_{\text{Prp}}=0.011$; mantle: $X_{\text{Sps}}=0.40$, $X_{\text{Alm}}=0.27$, $X_{\text{Grs}}=0.30$, $X_{\text{Prp}}=0.018$) constrain the growth of
304 garnet core and mantle at about 395 °C, 18.5 kbar (in the Chl + Grt + Act + Gln + Lws + Phe field) and 435°C,
305 19.5 kbar (in the Chl + Grt + Gln + Lws + Omp + Phe field) (Fig. 9a and Fig. SM4). The transition from the Act-
306 bearing (Omp-absent) field to the Omp-bearing (Act-absent) field is consistent with the occurrence of
307 actinolite inclusions within garnet core, and omphacite inclusions within garnet mantle. The modeled
308 phengite compositional isopleths (Si = 3.81-3.83 a.p.f.u.) constrain the growth of phengite at P-T conditions
309 slightly lower than the growth of garnet core.

310 The modeled garnet compositional isopleths from the fractionated pseudosection (rim: $X_{\text{Sps}}=0.24$,
311 $X_{\text{Alm}}=0.42$, $X_{\text{Grs}}=0.31$, $X_{\text{Prp}}=0.034$) constrain the growth of garnet rim at about 470 °C, 20 kbar (in the Chl +
312 Grt + Gln + Omp + Lws + Phe field) (Fig. 9a). The modeled modal amount of chlorite in equilibrium with
313 garnet rim is lower than 1 vol%.

314 Peak P-T conditions for sample 14-6F are therefore constrained at about 470 °C, 20 kbar. Overall, the
315 prograde P-T evolution of sample 14-6F is similar in shape to that predicted for sample 14-4B but at lower P
316 and slightly higher T (i.e. $\Delta T = + 50$ °C, $\Delta P = -2$ kbar). Similarly to sample 14-4B, the modeled isomodes do
317 not predict the growth (i.e. increase in modal amount) of lawsonite along this P-T path (Fig. 9b), opposite to
318 microstructural observation which clearly show that lawsonite grew simultaneously (or even later) to
319 garnet (Fig. 7).

320

321 5.2 The influence of Fe^{+3}

322 Although low, the Fe^{+3} content in glaucophane from both the samples is not negligible, suggesting that the
323 metasediment bulk compositions were slightly oxidized. In order to test the influence of Fe^{+3} on the
324 stability of the equilibrium assemblages and on the peak P-T conditions, two P- XFe_2O_3 and T- XFe_2O_3
325 pseudosections were calculated at 420°C, 22 kbar (sample 14-4B; Fig. 10a,b), and 470°C, 20 kbar (sample
326 14-6F; Fig. 10c,d), respectively, i.e. at the peak P-T conditions estimated for the two samples in the Fe^{+3} -free
327 MnNKCFMASH system. A XFe_2O_3 range of 0-0.5 was considered, with $\text{XFe}_2\text{O}_3 = \text{Fe}_2\text{O}_3/\text{FeO}_{\text{tot}}$ (i.e. $\text{XFe}_2\text{O}_3 = 0$
328 means that all Fe is bivalent; $\text{XFe}_2\text{O}_3 = 0.5$ means that FeO and Fe_2O_3 are present in equal amounts).

329 The P- XFe_2O_3 and T- XFe_2O_3 pseudosections modeled for sample 14-4B and contoured for the garnet rim
330 compositional isopleths, show that peak-P conditions decrease of about 2-3 kbar with increasing XFe_2O_3 ,
331 whereas peak-T conditions do not significantly change at variable XFe_2O_3 values. The XFe_2O_3 is constrained
332 to a maximum of 0.20, above which the modeled peak assemblage (Grt + Gln + Lws + Phe + minor Omp) is
333 no longer stable (Fig. 10a,b).

334 The same effects are also observed for sample 14-6F, but in this case the decrease of peak-P conditions is
335 less pronounced (ca. 1 kbar). The stability field of the peak assemblage (Grt + Gln + Omp + Lws + Phe +
336 minor Chl) constrains the maximum XFe_2O_3 value to 0.4, but for $\text{XFe}_2\text{O}_3 > 0.15$ the modeled garnet
337 compositional isopleths diverge, therefore constraining XFe_2O_3 to values in the range 0-0.15 (Fig. 10c,d).

338 The P-T paths of the two studied samples calculated for $X_{\text{Fe}_2\text{O}_3}=0.10$ mostly overlap, thus suggesting that
339 the prograde P-T evolution of the SSOM blueschists was characterized by an increase in P and T from ca.
340 370 °C, 17 kbar to peak conditions of ca. 470°C, 19 kbar.

341

342 **6. Discussion**

343 **6.1 H_2O -saturated vs. H_2O under-saturated conditions**

344 The results obtained so far are based on the assumption that H_2O was in excess during the whole
345 metamorphic evolution: this is a common assumption in the modeling of lawsonite-bearing blueschist and
346 eclogites (e.g. Davis and Whitney, 2006, 2008; Clarke et al., 2006; Groppo and Castelli, 2010; Endo et al.,
347 2012; Wei and Clarke, 2011; Vitale Brovarone et al., 2011; Ao and Bhowmik, 2014; Tian and Wei, 2014;
348 Bhowmik and Ao, 2015). In many cases H_2O is considered in excess because lawsonite-bearing assemblages
349 demand that high water amounts are available in the system. Opposite to this common assumption, it has
350 also been demonstrated that lawsonite can grow during subduction (at increasing P and T) at H_2O -
351 undersaturated conditions (e.g. Ballevre et al., 2003; Lopez-Carmona et al., 2013). H_2O -undersaturated
352 conditions would significantly influence phase equilibria and hence P-T estimates; therefore, the possibility
353 that prograde metamorphism could have occurred under H_2O -undersaturated conditions should be
354 carefully evaluated.

355 This issue was explored by calculating two P/T- $X(\text{H}_2\text{O})$ pseudosections for sample 14-4B (Fig. 11); similar
356 results are obtained for sample 14-6F (see Fig. 12a). These pseudosections report the H_2O content (in wt%)
357 on the horizontal axis and a P/T gradient on the vertical axis. Two P/T gradients have been considered: the
358 first one (gradient A: Fig. 11a) is coincident with the P-T path constrained using the P-T pseudosection
359 calculated with H_2O in excess, whereas the second one (gradient B: Fig. 11b) is steeper and similar to the
360 early prograde P-T evolution of Eastern Himalayan blueschists reported in the literature (Ao and Bhowmik.,
361 2014). The two pseudosections are contoured for garnet core and rim compositions. The intersection
362 between garnet compositional isopleths should provide information about: (i) whether the growth of
363 garnet with the measured composition could have occurred along the previously discussed P/T gradient A
364 but at H_2O -undersaturated conditions, and (ii) whether the alternative (steeper) P/T gradient B would be
365 compatible with the growth of garnet with the measured composition under H_2O -undersaturated
366 conditions.

367 The white dotted lines in the calculated P/T- $X(\text{H}_2\text{O})$ pseudosections represent the H_2O -saturation surface
368 and divide the pseudosections in a H_2O -saturated part on the right and in a H_2O -undersaturated part on the
369 left. A H_2O amount of 3-4 wt% (depending on T and P) is required to reach H_2O -saturated conditions in
370 sample 14-4B. Garnet compositional isopleths show that: (i) the steeper P/T gradient B (Fig. 11b) is not
371 compatible with the observed garnet compositions because the modeled compositional isopleths of garnet
372 core do not overlap; (ii) concerning the P/T gradient A, the intersection of garnet compositional isopleths
373 on the H_2O -saturation surface confirms that the growth of garnet with the measured composition occurred
374 at H_2O -saturated conditions (Fig. 11a, 12a), thus suggesting that the assumption of H_2O in excess for the
375 modeling of garnet growth was correct.

376

377 **6.2 When and how did lawsonite grow**

378 The P/T- $X(\text{H}_2\text{O})$ pseudosections calculated at H_2O saturated conditions for both samples 14-4B (Fig. 8) and
379 14-6F (Fig. 9) fail in modeling the contemporaneous growth of lawsonite and garnet; in fact, the inferred
380 prograde P-T path crosses the garnet isomodes upward (Fig. 8c, 9c), but the lawsonite isomodes are
381 crossed downward (Fig. 8b, 9b), thus suggesting that lawsonite was (slightly) consumed when garnet was
382 growing (i.e. lawsonite modal amount was slightly decreasing while garnet modal amount was increasing).

Two different hypothesis can be proposed to explain the discrepancy between the observed microstructures and the prediction of thermodynamic modeling: (i) the first hypothesis is still based on an equilibrium model for prograde metamorphism, which is the classical paradigm that is the basis of isochemical phase diagrams; (ii) the second hypothesis explores the possibility that the prograde appearance of lawsonite was controlled by nonequilibrium processes rather than by equilibrium ones (i.e. kinetics factors prevailing over equilibrium thermodynamics).

6.2.1 The equilibrium approach

Following an approach based on the principles of equilibrium thermodynamics, the P/T-X(H₂O) pseudosection calculated for sample 14-6F (Fig. 12a), contoured for lawsonite and garnet modal amounts (Fig. 12b, 12c) is useful to explain the inconsistency between the observed and predicted sequence of porphyroblasts growth (i.e. Lws contemporaneous with Grt vs. Lws earlier than Grt) (see also Fig. SM5 for sample 14-4B). Fig. 12b shows that H₂O addition is required to form lawsonite (i.e. to increase its modal amount). The observed microstructures suggest that lawsonite growth was contemporaneous to garnet growth (Fig. 7), thus implying that H₂O was introduced in the system at the relatively high pressure of ca. 17-18 kbar (large white arrow in Fig. 12b). Once reached H₂O-saturated conditions, garnet (with the measured composition of Grt core) started to form; the simultaneous growth of high modal amounts of lawsonite, however, subtracted H₂O to the system ("–H₂O" arrows in Fig. 12b), that eventually became again H₂O-undersaturated. A protracted H₂O influx at high pressure (" +H₂O" arrows in Fig. 12b) is therefore required in order to allow the contemporaneous growth of garnet (which requires H₂O-saturated conditions) and lawsonite (whose growth subtracts H₂O to the system).

Our model thus suggests that the system might have been H₂O-undersaturated during the early prograde subduction (i.e. prior to the appearance of garnet). According to the modeling, at H₂O-undersaturated conditions, the Ca-rich precursor of lawsonite should have been epidote: the small epidote inclusions observed in garnet porphyroblasts (sample 14-6F: Fig. 5f) would support this assumption. This hypothesis confirms what has been already predicted by previous studies, i.e. the H₂O-rich character of lawsonite-bearing assemblages requires the addition of H₂O at elevated pressure to allow them to form (Clarke et al., 2006; Tsujimori and Ernst, 2014). Significant fluid release is predicted at these P-T conditions (e.g. Ulmer and Trommsdorff, 1995; Scambelluri et al., 2004; Poli and Schmidt, 1995; Poli et al., 2009) through metamorphic devolatilization reactions occurring in the subducting slab (Bebout, 1991, 1995; Jarrad, 2003). Our results suggest that fluids released at P > 17-18 kbar by the de-hydrating subducting slab can be largely re-incorporated in lawsonite, and confirm that the pervasive growth of lawsonite represents an efficient mechanism for fixing water in the high pressure accretionary prism, thereby delaying its ascent toward the surface (Ballèvre et al., 2003; Vitale Brovarone and Beyssac, 2014).

6.2.2 The nonequilibrium approach

Alternatively to what discussed in the previous point, the inconsistency between the observed microstructures and the equilibrium phase relations predicted by the pseudosections could suggest that nonequilibrium processes controlled the prograde appearance of lawsonite and garnet. Transient nonequilibrium states can be common during prograde metamorphism (e.g. Ague & Carlson, 2013), especially at low temperatures such those inferred for the early prograde evolution of the studied blueschists. Previous works addressed the question of the interplay between the approach to equilibrium on one hand, and reaction kinetics on the other hand (see Ague & Carlson, 2013 for a review). Crucial to the discussion is the concept of reaction affinity, which is an energetic expression of the easiness of a reaction to overstep the kinetic barriers to nucleation and growth (e.g. Waters & Lovegrove, 2002; Pattison et al., 2011; Ketcham & Carlson, 2012). It has been demonstrated that mineral reactions which release large

quantities of H₂O have higher reaction affinity per unit of temperature/pressure overstep than those which release little or no H₂O. The former are expected to be overstepped in temperature and/or pressure less than the latter (see Pattison et al., 2011 for further details). Reactions with lower reaction affinity may be strongly influenced by kinetic factors, or may not occur at all.

Some authors considered nucleation as the main rate-limiting process in metamorphic reactions (e.g. Waters & Lovegrove, 2002; Gaidies et al., 2011; Pattison et al., 2011). They demonstrated that low reaction affinity (and consequently high overstepping) of a prograde metamorphic reaction may cause the delayed nucleation (and growth) of porphyroblastic phases. Microstructurally, this becomes evident when the observed sequence of porphyroblasts growth does not coincide with the sequence predicted by thermodynamic modelling (e.g. Waters & Lovegrove, 2002). Other authors argued that intergranular diffusion is the main kinetic component controlling the nucleation and growth of porphyroblastic phases (e.g. Carlson, 1989, 2002; Hirsch et al., 2000; Ketcham & Carlson, 2012). In this case, delayed porphyroblasts growth would be related to the sluggishness of intergranular diffusion. More in detail, growing porphyroblasts extract nutrients from the immediate surroundings, suppressing the nucleation of new crystals in diffusionally depleted zones surrounding pre-existing crystals.

A quantitative treatment of these concepts is well beyond the aim of this paper; nevertheless, it is worth noting that the modelled pseudosection for sample 14-6F predicts that lawsonite is mainly produced at low P-T conditions (i.e. at P < 5 kbar, and T < 300°C; Fig. SM6) through the epidote or prehnite (depending on T) breakdown, much earlier than the onset of garnet growth. Both the epidote- and prehnite-consuming (lawsonite-producing) reactions are hydration reactions, i.e. they consume H₂O. Qualitatively, it is therefore to be expected that reaction affinity of these reactions is very low and that they might be significantly overstepped in temperature and pressure. The discrepancy between the observed and predicted sequence of porphyroblasts growth can be therefore explained by a delayed growth of lawsonite porphyroblasts, possibly due to: (i) low reaction affinity of the Lws-producing reaction (either Ep- or Prh-consuming), and/or (ii) difficulty of nucleation of lawsonite.

Both the equilibrium- and nonequilibrium- hypothesis are compatible with microstructural observations (e.g. the rare occurrence of small epidote inclusions within garnet) and they are complementary rather than mutually exclusive.

6.3 Interpretation of the P-T evolution and geodynamic implications

Prior to this study, P-T estimates based on conventional thermobarometry suggested peak P-T conditions of 350-420°C, 9-11 kbar for the SSOM blueschists (Honegger et al., 1989). The results of our petrological modeling point to peak P-T conditions significantly higher than those previously estimated, i.e. ca. 470°C, 19 kbar (Fig. 13), thus suggesting that the careful re-examination (by means of modern petrological approaches) of previous P-T estimates obtained using conventional thermobarometry can provide new insights on the subduction history of the Neo-Tethyan ocean. The obtained results suggest that the SSOM blueschists experienced a cold subduction history along a very low to low thermal gradient ("early" prograde: ca. 5-6°C/km; "late" prograde: ca. 7-8°C/km; Fig. 13a). Furthermore, in order to preserve lawsonite in the studied lithologies, exhumation must have been coupled with significant cooling (i.e. without crossing the lawsonite-out boundary; Zack et al., 2004). The resulting P-T path is therefore characterized by a clockwise hairpin loop along low thermal gradients (< 8-9 °C/km) (Fig. 13a).

This P-T evolution is consistent with a cold subduction zone system in an intra-oceanic subduction setting, as also suggested by Ao and Bhowmik (2014) for blueschists from the far eastern Himalaya. Moreover, the observed lithological associations (i.e. mainly volcanoclastic rocks and minor sediments), the estimated peak P-T conditions (very close to the eclogite stability field but still inside the lawsonite blueschist -facies) and the clockwise hairpin P-T trajectory, are all consistent with the interpretation that the SSOM represents

a relic of an oceanic paleo-accretionary prism, related to the northward subduction of the northern Neo-Tethyan ocean beneath the Ladakh Asian margin (Robertson, 2000; Mahéo et al., 2006; Guillot et al., 2008). Interestingly, the estimated peak P-T conditions of ca. 470°C, 19 kbar roughly coincide with the maximum P-T estimates predicted by thermo-mechanical models for the metasediments exhumed in the accretionary wedge (Yamato et al. 2007) (Fig. 13a), and with the maximum P-T conditions registered by natural occurrences of blueschist accretionary complexes worldwide (Fig. 13b) (e.g. the Schistes Lustres Complex of the Western Alps and Alpine Corsica, Turkey, Zagros, Oman, New Caledonia, Franciscan Complex: e.g. Banno et al., 2000; Agard et al., 2001a,b; Warren et al., 2005; Agard et al., 2006; Page et al., 2006; Tsujimori et al., 2006; Warren and Waters, 2006; Ernst and McLaughlin, 2012; Plunder et al., 2012, 2015; Agard and Vitale Brovarone, 2013; Ukar and Cloos, 2014; Vitale Brovarone et al., 2014). Most of the studies focused on subduction-related HP-LT terranes from different localities point to a continuous increase of peak-T and associated P in adjacent tectonometamorphic units (Fig. 13b). A continuous metamorphic gradient is thus recorded in most of the blueschist-facies terranes worldwide, up to maximum P-T conditions of ca. 470°C, 18-19 kbar (e.g. Oman: Yamato et al., 2007; Corsica: Vitale Brovarone et al., 2014; Schistes Lustres of the Western Alps: Plunder et al., 2012; New Caledonia: Vitale Brovarone & Agard, 2013; Turkey: Plunder et al., 2015). This metamorphic zonation might reflect the repeated accretion of the ocean-floor sediments subducted at different depths and offscraped at the base of the accretionary prism (e.g. Agard et al., 2009 and references therein). A similar metamorphic zonation from greenschist to pumpellyite-diopside and up to lawsonite-blueschist - facies conditions has been recently reported by Ao & Bhowmik (2014) for the Nagaland Ophiolite Complex of far-eastern Himalaya, whose geological setting is very similar to that of the SSOM (i.e. it is mainly dominated by metavolcanoclastic rocks, with minor intercalations of metasediments). Although a detailed discussion of the SSOM metamorphic units adjacent to the blueschist one is beyond the aim of this paper, it is worth mentioning that preliminary data suggest that a similar metamorphic zonation might characterize also the western portion of the ITS zone. Chlorite + epidote + green/blue-green amphibole -bearing metavolcanoclastic rocks, and prehnite-pumpellyite -bearing metagabbros occur in the thin metamorphic slices associated to the blueschist unit in the SSOM. Further petrological investigations could eventually confirm the existence of a continuous metamorphic gradient in the SSOM.

503
504

505 **Acknowledgements**

506 This study is part of a Cooperation Agreement between the University of Torino, Dept. of Earth Sciences
507 (Torino, Italy) and the Wadia Institute of Himalayan Geology (Dehradun, India). Fieldwork was supported by
508 University of Torino—Call 1—Junior PI Grant (TO_Call1_2012_0068); laboratory work was supported by the
509 Italian Ministry of University and Research (PRIN 2011 - 2010PMKZX7) and Ricerca Locale (ex-60% - 2014)
510 funds of the University of Torino. We thank A. Vitale Brovarone for useful discussions on lawsonite-bearing
511 rocks. Constructive reviews from S. Guillot and an anonymous reviewer improved the final manuscript.

512 References

- 513 Abers, G.A., Nakajima, J., van Keken, P.E., Kita, S., Hacker, B.R., 2013. Thermal-petrological controls on the
514 location of earthquakes within subducting plates. *Earth and Planetary Science Letters* 369–370, 178–187.
- 515 Acharyya, S.K., 1986. Tectono-stratigraphic history of Naga Hills Ophiolites, in: Ghosh, D.B. (ed.), *Geology of*
516 *the Nagaland Ophiolite*. Geological Survey of India Memoirs 119, 94-103.
- 517 Agard, P., Monié, P., Gerber, W., Omrani, J., Molinaro, M., Meyer, B., Labrousse, L., Vrielynck, B., Jolivet, L.,
518 Yamato, P., 2006. Transient, syn-obduction exhumation of Zagros blueschists inferred from P–T-
519 deformation-time and kinematic constraints: implications for Neotethyan wedge dynamics. *Journal of*
520 *Geophysical Research* 111, B11401.
- 521 Agard, P., Jolivet, L., Goffé, B., 2001a. Tectonometamorphic evolution of the Schistes Lustrés complex:
522 implications for the exhumation of HP and UHP rocks in the Western Alps. *Bulletin de la Société*
523 *Geologique de France* 172, 617-636.
- 524 Agard, P., Vidal, O., Goffé, B., 2001b. Interlayer and Si content of phengite in carpholite-bearing
525 metapelites. *Journal of Metamorphic Geology* 19, 479-495.
- 526 Agard, P., Vitale-Brovarone, A., 2013. Thermal regime of continental subduction: the record from exhumed
527 HP-LT terranes (New Caledonia, Oman, Corsica). *Tectonophysics* 601, 206-215.
- 528 Agard, P., Yamato, P., Jolivet, L., Burov, J.E., 2009. Exhumation of oceanic blueschists and eclogites in
529 subduction zones: timing and mechanisms. *Earth Science Reviews* 92, 53-79.
- 530 Ague, J.J., Carloson, W.D., 2013. Metamorphism as garnet sees it: the kinetics of nucleation and growth,
531 equilibration and diffusional relaxation. *Elements* 9, 439-445.
- 532 Ahmad, T., Islam, R., Khanna, P., Thakur, V.C., 1996. Geochemistry, petrogenesis and tectonic significance
533 of the basic volcanic units of the Zildat ophiolite mélange, Indus suture zone, eastern Ladakh (India).
534 *Geodinamica Acta* 9, 222-233.
- 535 Ao, A., Bhowmik, S.K., 2014. Cold subduction of the Neotethys: the metamorphic record from finely
536 banded lawsonite and epidote blueschists and associated metabasalts of the Nagaland Ophiolite
537 Complex, India. *Journal of Metamorphic Geology* 32, 829-860.
- 538 Ballèvre, M., Pitra, P., Bohn, M., 2003. Lawsonite growth in the epidote blueschists from the Ile de Groix
539 (Armorican Massif, France): a potential geobarometer. *Journal of Metamorphic Geology* 21, 723-735.
- 540 Banno, S., Shibakusa, H., Enami, M., Wang, C.-L., Ernst, W.G., 2000. Chemical fine structure of Franciscan
541 jadeitic pyroxene from Ward Creek, Cazadero area, California. *American Mineralogist* 85, 1795-1798.
- 542 Bebout, G.E., 1991. Field-based evidence for devolatilization in subduction zones: implications for arc
543 magmatism. *Science* 251, 413–416.
- 544 Bebout, G.E., 1995. The impact of subduction-zone metamorphism on mantle-ocean chemical cycling.
545 *Chemical Geology* 126, 191-218.
- 546 Bebout, G.E., 2007. Metamorphic chemical geodynamics of subduction zones. *Earth and Planetary Science*
547 *Letters* 260, 373-393.
- 548 Bhowmik, S., Ao, A., 2015. Subduction initiation in the Neo-Tethys: constraints from counterclockwise P-T
549 paths in amphibolite rocks of the Nagaland Ophiolite Complex, India. *Journal of Metamorphic Geology*,
550 doi: 10.1111/jmg.12169
- 551 Cannat, M., Mascle, G., 1990. Réunion extraordinaire de la société géologique de France en Himalaya du
552 Ladakh. *Bulletin de la Société Géologique de France* 4, 553-582.
- 553 Cao, Y., Jung, H., Song, S., 2013. Petro-fabrics and seismic properties of blueschist and eclogite in the North
554 Qilian suture zone, NW China. Implications for the low-velocity upper layer in subducting slab, trench-
555 parallel seismic anisotropy and eclogite detectability in the subduction zone. *Journal of Geophysical*
556 *Research* 118, 3037–3058.

Carlson, W.D., 1989. The significance of intergranular diffusion to the mechanisms and kinetics of porphyroblast crystallization. *Contribution to Mineralogy and Petrology* 103, 1-24.

Carlson, W.D., 2002. Scales of disequilibrium and rates of equilibration during metamorphism. *American Mineralogist* 87, 185-204.

Chakungal, J., Dostal, J., Grujic, D., Duchêne, S., Ghalley, S.K., 2010. Provenance of the Greater Himalayan Sequence: Evidence from mafic eclogite-granulites and amphibolites in NW Bhutan. *Tectonophysics* 480, 198-212.

Chantel, J., Mookherjee, M., Frost, D.J., 2012. The elasticity of lawsonite at high pressure and the origin of low velocity layers in subduction zones. *Earth and Planetary Science Letters* 349–350, 116-125.

Chatterjee, N., Ghose, N.C., 2010. Metamorphic evolution of the Naga Hills eclogite and blueschist, Northeast India: implications for early subduction of the Indian plate under the Burma microplate. *Journal of Metamorphic Geology* 28, 209-225.

Clarke, G.L., Powell, R., Fitzherbert, J.A., 2006. The lawsonite paradox: a comparison of field evidence and mineral equilibria modeling. *Journal of Metamorphic Geology* 24, 716-726.

Connolly, J.A.D., 1990. Multivariable phase diagrams: an algorithm based on generalized thermodynamics. *American Journal of Science* 290, 666-718.

Connolly, J.A.D., 2009. The geodynamic equation of state: what and how. *Geochemistry Geophysics Geosystems* 10, Q10014.

Cossio, R., Borghi, A., Ruffini, R., 2002. Quantitative modal determination of geological samples based on X-ray multielemental map acquisition. *Microscopy and Microanalysis* 8, 139-149.

Davis, P.B., 2011. Petrotectonics of lawsonite eclogite exhumation: Insights from the Sivrihisar massif, Turkey. *Tectonics* 30, TC1006.

Davis, P.B., Whitney, D.L., 2006. Petrogenesis of lawsonite and epidote eclogite and blueschist, Sivrihisar, Turkey. *Journal of Metamorphic Geology* 24, 823-849.

Davis, P.B., Whitney, D.L., 2008. Petrogenesis and structural petrology of high-pressure metabasalt pods, Sivrihisar, Turkey. *Contributions to Mineralogy and Petrology* 156, 217-241.

De Sigoyer, J., Chavagnac, V., Blichert-Toft, J., Villa, I.M., Luais, B., Guillot, S., Cosca, M., Mascle, G., 2000. Dating the Indian continental subduction and collisional thickening in the northwest Himalaya: multichronology of the Tso Moriri eclogites. *Geology* 28, 487-490.

De Sigoyer, J., Guillot, S., Dick, P., 2004. Exhumation Processes of the high pressure low-temperature Tso Moriri dome in a convergent context (eastern-Ladakh, NW-Himalaya). *Tectonics* 23, TC3003.

Diener, J.F.A., Powell, R., 2012. Revised activity-composition models for clinopyroxene and amphibole. *Journal of Metamorphic Geology* 30, 131–142.

Diener, J.F.A., Powell, R., White, R.W., Holland, T.J.B., 2007. A new thermodynamic model for clino- and orthoamphiboles in the system $\text{Na}_2\text{O}-\text{CaO}-\text{FeO}-\text{MgO}-\text{Al}_2\text{O}_3-\text{SiO}_2-\text{H}_2\text{O}-\text{O}$. *Journal of Metamorphic Geology* 25, 631-656.

Endo, S., Wallis, S.R., Tsuboi, M., Torres de Leon, R., Solari, A., 2012. Metamorphic evolution of lawsonite eclogites from the southern Motagua fault zone, Guatemala: insights from phase equilibria and Raman spectroscopy. *Journal of metamorphic geology* 30, 143-164.

Ernst, W.G., 1988. Tectonic history of subduction zones inferred from retrograde blueschist P–T paths. *Geology* 16, 1081-1084.

Ernst, W.G., McLaughlin, R.J., 2012. Mineral parageneses, regional architecture, and tectonic evolution of Franciscan metagraywackes, Cape Mendocino-Garberville-Covelos 30' × 60' quadrangles, northwest California. *Tectonics* 31, TC1001.

601 Fitzherbert, J.A., Clarke, G.L., Marmo, B., Powell, R., 2004. The Origin and P–T evolution of peridotites and
 602 serpentinites of NE New Caledonia: prograde interaction between continental margin and the mantle
 603 wedge. *Journal of Metamorphic Geology* 22, 327-344.

604 Fitzherbert, J.A., Clarke, G.L., Powell, R., 2005. Preferential retrogression of high-P metasediments and the
 605 preservation of blueschist to eclogite facies metabasite during exhumation, Diahot terrane, NE New
 606 Caledonia. *Lithos* 83, 67-96.

607 Fitzherbert, J.A., Clarke, G.L., Powell, R., Powell, R., 2003. Lawsonite-omphacite-bearing metabasites of the
 608 Pam Peninsula, NE New Caledonia: evidence for disrupted blueschist- to eclogite-facies conditions.
 609 *Journal of Petrology* 44, 1805-1831.

610 Frank, W., Gansser, A., Trommsdorff, V., 1977. Geological observations in the Ladakh area (Himalayas): a
 611 preliminary report. *Schweizerische Mineralogische und Petrographische Mitteilungen* 57, 89-113.

612 Gaidies, F., Pattison, D.R.M., de Capitani, C., 2011. Toward a quantitative model of metamorphic nucleation
 613 and growth. *Contribution to Mineralogy and Petrology* 162, 975-993.

614 Ghose, N.C., Singh, R.N., 1980. Occurrence of blueschist facies in the ophiolite belt of Naga Hills, east of
 615 Kiphire, N.E., India. *Geologische Rundschau* 69, 41-43.

616 Green, E.C.R., Holland, T.J.B., Powell, R., 2007. An order-disorder model for omphacitic pyroxenes in the
 617 system jadeite-diopside-hedenbergite-acmite, with applications to eclogite rocks. *American Mineralogist*
 618 92, 1181-1189.

619 Groppo, C., Castelli, D., 2010. Prograde P–T evolution of a lawsonite eclogite from the Monviso meta-
 620 ophiolite (Western Alps): dehydration and redox reactions during subduction of oceanic FeTi-oxide
 621 gabbro. *Journal of Petrology* 51, 2489-2514.

622 Groppo, C., Lombardo, B., Rolfo, F., Pertusati, P., 2007. Clockwise exhumation path of granulitized eclogites
 623 from the Ama Drime range (Eastern Himalayas). *Journal of Metamorphic Geology* 25, 51-75.

624 Grujic, D., Warren, C., Wooden, J.L., 2011. Rapid synconvergent exhumation of Miocene-aged lower
 625 orogenic crust in the eastern Himalaya. *Lithosphere* 3, 346-366.

626 Guillot, S., Cosca, M., Allemand, P., Le Fort, P., 1999. Contrasting metamorphic and geochronologic
 627 evolution along the Himalayan belt, in: Macfarlane, A., Sorkhabi, R.B., Quade, J. (Eds.), *Himalaya and
 628 Tibet: Mountain Roots to Mountain Tops*. Geological Society of America, Boulder, Colorado. Special
 629 Paper, pp. 330.

630 Guillot, S., de Sigoyer, J., Lardeaux, J.M., Mascle, G., 1997. Eclogitic metasediments from the Tso Moriri
 631 area (Ladakh, Himalaya): evidence for continental subduction during India–Asia convergence.
 632 *Contribution to Mineralogy and Petrology* 128, 197-212.

633 Guillot, S., Mahéo, G., de Sigoyer, J., Hattori, K.H., Pecher, A., 2008. Tethyan and Indian subduction viewed
 634 from the Himalayan high- to ultrahigh-pressure metamorphic rocks. *Tectonophysics* 451, 225-241.

635 Guillot, S., Replumaz, A., Hattori, K., Strzeczynski, P., 2007. Initial geometry of western Himalaya and
 636 ultrahigh pressure metamorphic evolution. *Journal of Asian Earth Sciences* 30, 557-564.

637 Guiraud, M., 1982. *Géothermométrie du faciès schistes vert à glaucophane. Modélisation et applications*.
 638 University of Montpellier. Ph.D.

639 Guiraud, M., Powell, R., Rebay, G., 2001. H₂O in metamorphism and unexpected behavior in the
 640 preservation of metamorphic mineral assemblages. *Journal of Metamorphic Geology* 19, 445-454.

641 Hacker, B.R., 2008. H₂O subduction beyond arcs. *Geochemistry Geophysics Geosystems* 9, B03204.

642 Hacker, B.R., Abers, G. A., Peacock, S. M., 2003. Subduction factory 1. Theoretical mineralogy, densities,
 643 seismic wave speeds, and H₂O contents. *Journal of Geophysical Research* 108, 2029.

644 Hirsch, D.M., Ketchum, R.A., Carlson, W.D., 2000. An evaluation of spatial correlation functions in textural
 645 analysis of metamorphic rocks. *Geological Material Research* 2, 1-21.

646 Holland, T., Baker, J., Powell, R., 1998. Mixing properties and activity-composition relationships of chlorites
 647 in the system $\text{MgO-FeO-Al}_2\text{O}_3\text{-SiO}_2\text{-H}_2\text{O}$. *European Journal of Mineralogy* 10, 395-406.
 648 Holland, T.J.B., Powell, R., 1998. An internally consistent thermodynamic dataset for phases of petrological
 649 interest. *Journal of Metamorphic Geology* 16, 309-343.
 650 Honegger, K., Le Fort, P., Mascle, G., Zimmerman, J.L., 1989. The blueschists along the Indus Suture zone in
 651 Ladakh, NW Himalaya. *Journal of Metamorphic Geology* 7, 57-72.
 652 Jan, M.Q., 1985. High-P rocks along the suture zone around Indo-Pakistan plate and phase chemistry of
 653 blueschists from eastern Ladakh. *Geological Bulletin University of Peshawar* 18, 1-40.
 654 Jan, M.Q., 1987. Phase chemistry of blueschists from eastern Ladakh, Himalaya. *Neues Jahrbuch fuer*
 655 *Geologie und Palaeontologie* 10, 613-635.
 656 Jarrard, R.D., 2003. Subduction fluxes of water, carbon dioxide, chlorine, and potassium. *Geochemistry*
 657 *Geophysics Geosystems* 4, 8905.
 658 Jolivet, L., Faccenna, C., Goffé, B., Burov, E., Agard, P., 2003. Subduction tectonics and exhumation of high-
 659 pressure metamorphic rocks in the Mediterranean orogens. *American Journal of Science* 303, 353-409.
 660 Ketcham, R.A., Carlson, W.D., 2012. Numerical simulation of diffusion-controlled nucleation and growth of
 661 porphyroblasts. *Journal of Metamorphic Geology* 30, 489-512.
 662 Kim, D., Katayama, I., Michibayashi, K., Tsujimori, T., 2013. Deformation fabrics of natural blueschists and
 663 implications for seismic anisotropy in subducting oceanic crust. *Physics of the Earth and Planetary*
 664 *Interiors* 222, 8-21.
 665 Lanari, P., Riel, N., Guillot, S., Vidal, O., Schwartz, S., Pêcher, A., Hattori, K.H., 2013. Deciphering high-
 666 pressure metamorphism in collisional context using microprobe mapping methods: Application to the
 667 Stak eclogitic massif (northwest Himalaya). *Geology* 41, 111-114.
 668 Leake, B.F., Woolley, A.R., Arps, C.E.S. et al., 1997. Nomenclature of amphiboles: report of the
 669 subcommittee on amphiboles of the International Mineralogical Association, commission on new
 670 minerals and mineral names. *American Mineralogist* 82, 1019-1037.
 671 Lombardo, B., Rolfo, F., 2000. Two contrasting eclogite types in the Himalayas: implications for the
 672 Himalayan orogeny. *Journal of Geodynamics* 30, 37-60.
 673 Lopez-Carmona, A., Pitra, P., Abati, J., 2013. Blueschist- facies metapelites from the Malpica-Tui Unit (NW
 674 Iberian Massif): phase equilibria modelling and H_2O and Fe_2O_3 influence in high-pressure assemblages.
 675 *Journal of Metamorphic Geology* 31, 263-280.
 676 Mahéo, G., Fayoux, C., Guillot, S., Garzanti, E., Capiez, P., Mascle, G., 2006. Geochemistry of ophiolitic rocks
 677 and blueschists from the Sapi-Shergol mélange (Ladakh, NW Himalaya, India): implication for the timing
 678 of the closure of the Neo-Tethys ocean. *Journal of Asian Earth Sciences* 26, 695-707.
 679 Martin, L.A.J., Wood, B.J., Turner, S., Rushmer, T., 2011. Experimental measurements of trace element
 680 partitioning between lawsonite, zoisite and fluid and their implication for the composition of arc
 681 magmas. *Journal of Petrology* 52, 1049-1075.
 682 Newton, R.C., Charlu, T.V., Kleppa, O.J., 1980. Thermochemistry of the high structural state plagioclases.
 683 *Geochimica and Cosmochimica Acta* 44, 933-941.
 684 O'Brien, P.J., Zotov, N., Law, R., Khan, A.M., 2001. Coesite in Himalaya eclogite and implications for models
 685 of India-Asia collision. *Geology* 29, 435-438.
 686 Page, F.Z., Armstrong, L.S., Essene, E.J., Mukasa, S.B., 2006. Prograde and retrograde history of the Junction
 687 School eclogite, California, and an evaluation of garnet-phengite-clinopyroxene thermobarometry.
 688 *Contribution to Mineralogy and Petrology* 153, 533-555.
 689 Pattison, D.R.M., de Capitani, C., Gaidies, F., 2011. Petrological consequences of variations in metamorphic
 690 reaction affinity. *Journal of Metamorphic Geology* 29, 953-977.

691 Plunder, A., Agard, P., Chopin, C., Pourteau, A., Okay, A.I., 2015. Accretion, underplating and exhumation
692 along a subduction interface: From subduction initiation to continental subduction (Tavşanlı zone, W.
693 Turkey). *Lithos* 226, 233-254.

694 Plunder, A., Agard, P., Dubacq, B., Chopin, C., Bellanger, M., 2012. How continuous and precise is the record
695 of P-T paths? Insights from combined thermobarometry and thermodynamic modelling into subduction
696 dynamics (Schistes Lustrés, W. Alps). *Journal of Metamorphic Geology* 30, 323-346.

697 Pognante, U., Spencer, D.A., 1991. First report of eclogites from the Himalayan belt, Kaghan valley
698 (northern Pakistan). *European Journal of Mineralogy* 3, 613-618.

699 Poli, S., Franzolin, E., Fumagalli, P., Crottini, A., 2009. The transport of carbon and hydrogen in subducted
700 oceanic crust: An experimental study to 5 GPa. *Earth and Planetary Science Letters* 278, 350-360.

701 Poli, S., Schmidt, M.W., 1995. H₂O transport and release in subduction zones: Experimental constraints on
702 basaltic and andesitic systems. *Journal of Geophysical Research* 100, 22299-22314.

703 Pouchou, J.L., Pichoir, F., 1988. Determination of mass absorption coefficients for soft X-Rays by use of the
704 electron microprobe. *Microbeam Analysis*, San Francisco Press, pp 319-324.

705 Ravna, E.J.K., Andersen, B., Jolivet, L., De Capitani, C., 2010. Cold subduction and the formation of lawsonite
706 eclogite – constraints from prograde evolution of eclogitized pillow lava from Corsica. *Journal of*
707 *Metamorphic Geology* 28, 381-395.

708 Reuber, I., Colchen, M., Mevel, C., 1987. The geodynamic evolution of the south-Tethyan margin in Zaskar,
709 NW Himalaya, as revealed by the Spontang ophiolitic mélange. *Geodinamica Acta* 1, 283-296.

710 Robertson, A., 2000. Formation of mélanges in the Indus Suture Zone, Ladakh Himalaya by successive
711 subduction-related, collisional and post-collisional processes during Late Mesozoic–Late Tertiary time, in:
712 Khan, M.A., Treolar, P.J., Searle, M.P., Jan, Q. (Eds.), *Tectonics of the Nanga Parbat Syntaxis and the*
713 *Western Himalaya*. Geological Society of London Special Publication 170, 333-374.

714 Sachan, H.K., Mukherjee, B.K., Ogasawara, Y., Maruyama, S., Ishida, H., Muko, A., Yoshioka, N., 2004.
715 Discovery of coesite from Indus Suture Zone (ISZ), Ladakh, India: Evidence for deep subduction. *European*
716 *Journal of Mineralogy* 16, 235-240.

717 Scambelluri, M., Müntener, O., Ottolini, L., Pettke, T., Vannucci, R., 2004. The fate of B, Cl and Li in the
718 subducted oceanic mantle and in the antigorite breakdown fluids. *Earth and Planetary Science Letters*
719 222, 217-234.

720 Schumacher, J.C., Brady, J.B., Cheney, J.T., Tonnsen, R.R., 2008. Glaucofane-bearing marbles on Syros,
721 Greece. *Journal of Petrology* 49, 1667-1686.

722 Shams, F.A., 1972. Glaucofane-bearing rocks from near Topsin, Swat. First record from Pakistan. *Pakistan*
723 *Journal of Scientific Research* 24, 343-345.

724 Socquet, A., Goffé, B., Pubellier, M., Rangin, C., 2002. Le métamorphisme Tardi-Crétacé à Éocène des zones
725 internes de la chaîne Indo-Birmannaise (Myanmar occidentale): Implications géodynamiques. *Comptes Rendus*
726 *Geoscience* 334, 573-580.

727 Spandler, C., Pirard, C., 2013. Element recycling from subducting slabs to arc crust: A review. *Lithos* 170-
728 171, 208-223.

729 Sutra, E., 1990. Les formations de la marge nord-neotéthysienne et les mélanges ophiolitiques de la zone
730 de suture de l'Indus en Himalaya du Ladakh, Inde. PhD Thesis, Poitiers University, France, pp. 662.

731 Tian, Z.L., Wei, C.J., 2014. Coexistence of garnet blueschist and eclogite in South Tianshan, NW China:
732 dependence of P–T evolution and bulk-rock composition. *Journal of Metamorphic Geology* 32, 743-764.

733 Tsujimori, T., Ernst, W.G., 2014. Lawsonite blueschists and lawsonite eclogites as proxies for palaeo-
734 subduction zone processes: a review. *Journal of Metamorphic Geology* 32, 437–454.

735 Tsujimori, T., Matsumoto, K., Wakabayashi, J., Liou, J.G., 2006. Franciscan eclogite revisited: re-evaluation
736 of the P–T evolution of tectonic blocks from Tiburon Peninsula, California, USA. *Mineralogy and*
737 *Petrology* 88, 243-267.

738 Ukar, E., Cloos, M., 2014. Low-temperature blueschist-facies mafic blocks in the Franciscan melange, San
739 Simeon, California: Field relations, petrology, and counterclockwise P-T paths. *Geological Society of*
740 *America Bulletin* 126, 831-856.

741 Ulmer, P., Trommsdorff, V., 1995. Serpentine stability to mantle depths and subduction related
742 magmatism. *Science* 268, 858-861.

743 Vidal, O., Parra, T., 2000. Exhumation paths of high-pressure metapelites obtained from local equilibria for
744 chlorite- phengite assemblages. *Geological Journal* 35, 139-161.

745 Viridi, N.S., Thakur, V.C., Kumar, S., 1977. Blueschist facies metamorphism from the Indus suture zone of
746 Ladakh and its significance. *Himalaya Geology* 7, 479-482.

747 Vitale Brovarone, A., Agard, P., 2013. True metamorphic isograds or tectonically sliced metamorphic
748 sequence? New high-spatial resolution petrological data for the New Caledonia case study. *Contributions*
749 *to Mineralogy and Petrology* 166, 451-469.

750 Vitale Brovarone, A., Alard, O., Beyssac, O., Picatto, M., 2014. Lawsonite metasomatism and trace element
751 recycling in subduction zones. *Journal of Metamorphic Geology* 32, 489-514.

752 Vitale Brovarone, A., Beyssac, O., 2014. Lawsonite metasomatism: A new route for water to the deep Earth.
753 *Earth and Planetary Science Letters* 393, 275-284.

754 Vitale Brovarone, A., Beyssac, O., Malavieille, J., Molli, G., Beltrando, M., Compagnoni, R., 2013. Stacking
755 and metamorphism of continuous segments of subducted lithosphere in a high-pressure wedge: The
756 example of Alpine Corsica (France). *Earth-Science Reviews* 116, 35-56.

757 Vitale Brovarone, A., Groppo, C., Hetenyi, G., Compagnoni, G., Malavieille, J., 2011. Coexistence of
758 lawsonite-bearing eclogite and blueschist: phase equilibria modelling of Alpine Corsica metabasalts and
759 petrological evolution of subducting slabs. *Journal of Metamorphic Geology* 29, 583-600.

760 Warren, C.J., Grujic, D., Kellett, D.A., Cottle, J., Jamieson, R.A., Ghalley, K.S., 2011. Probing the depths of the
761 India-Asia collision: U-Th-Pb monazite chronology of granulites from NW Bhutan. *Tectonics* 30, TC2004.

762 Warren, C.J., Parrish, R.R., Waters, D.J., Searle, M.P., 2005. Dating the geologic history of Oman's Semail
763 ophiolite: insights from U–Pb geochronology. *Contributions to Mineralogy and Petrology* 150, 403-422.

764 Warren, C.J., Waters, D.J., 2006. Oxidized eclogites and garnet–blueschists from Oman: P–T path modeling
765 in the NCFMASHO system. *Journal of Metamorphic Geology* 24, 783-802.

766 Waters, D.J., Lovegrove, D.P., 2002. Assessing the extent of disequilibrium and overstepping of prograde
767 metamorphic reactions in metapelites from the Bushveld Complex aureole, South Africa. *Journal of*
768 *Metamorphic Geology* 20, 135-149.

769 Wei, C.J., Clarke, G.L., 2011. Calculated phase equilibria for MORB compositions: a reappraisal of the
770 metamorphic evolution of lawsonite eclogite. *Journal of Metamorphic Geology* 29, 939-952.

771 Yamato, P., Agard, P., Burov, E., Le Pourhiet, L., Jolivet, L., Tiberi, C., 2007. Burial and exhumation in a
772 subduction wedge: mutual constraints from thermo-mechanical modeling and natural P-T-t data
773 (Schistes Lustrés, W. Alps). *Journal of Geophysical Research* 112, B07410.

774 Zack, T., Rivers, T., Brumm, R., Kronz, A., 2004. Cold subduction of oceanic crust: Implications from a
775 lawsonite eclogite from the Dominican Republic. *European Journal of Mineralogy* 16, 909-916.

776

777 **Figure captions**

778 **Fig. 1** – Geological sketch map of the studied area (modified after Honegger et al., 1989). (1) Dras-Naktul
 779 volcanoclastics and flysch; (2) pillow lavas, sill and dyke series; (3) ultramafic lenses; (4) Shergol
 780 conglomerate; (5) mèlange formation; (6) blueschist zone; (7) Karamba and Lamayuru unit; (8) Zaskar unit.
 781 Star: samples location. Inset: simplified tectonic map of the Himalayan orogen showing the locations of the
 782 blueschist facies rocks in the Indus Tsangpo suture zone (ITS). 1, Shangla; 2, Sapi-Shergol; 3, Zildat; 4, Sans
 783 Sang; 5, Yamdrock; 6, Nagaland. Other abbreviations used: NP, Nanga Parbat; NB, Namche Barwa; MBT,
 784 Main Boundary Thrust; MFT, Main Frontal Thrust.

785
 786 **Fig. 2** – (a) Panoramic view of the Sapi-Shergol Ophiolite Melange (in blue). View looking north-westward.
 787 Landscape width is about 20 km. (b,c) Outcrop appearance of the most abundant blueschist lithologies in
 788 the SSOM: volcanoclastic rocks (b) and metabasic rocks (c). (d-g) Representative microstructures of
 789 volcanoclastic (d) and metabasic (e) rocks and of silicic (f) and carbonatic (g) metasediments. The dotted
 790 white line in (d) separates a pluri-mm clast (lower right) from the reddish matrix (upper left). The inset in
 791 (g) shows a detail of a large poikiloblast of calcite including idioblastic lawsonite. Plane Polarized Light (PPL).
 792

793 **Fig. 3** - Processed major elements μ -XRF maps of the whole thin sections of samples 14-4B and 14-6F. The
 794 unprocessed μ -XRF maps for each element are reported in Fig. SM1 and SM2.

795
 796 **Fig. 4** – Representative microstructures of sample 14-4B. (a) Detail of a discontinuous quartz-rich layer
 797 alternated to thicker lawsonite + phengite + glaucophane layers. Note the small dark garnet on the right.
 798 (PPL). (b, c) Detail of a phengite + lawsonite + glaucophane layer: phengite and glaucophane define the
 799 main foliation. PPL (b) and Crossed Polarized Light (XPL) (c).
 800

801 **Fig. 5** – Representative microstructures of sample 14-6F/G. (a) The main foliation, defined by the preferred
 802 orientation of glaucophane and minor phengite, is overgrown by large lawsonite and garnet porphyroblasts
 803 and is intensely crenulated. PPL (a), XPL (b). (c) Detail of a boudinated lawsonite porphyroblast overgrowing
 804 the fine-grained glaucophane + phengite matrix. Lawsonite and quartz occur in the pressure shadows. Note
 805 the garnet porphyroblasts, overgrowing the main foliation and included in lawsonite. PPL. (d) Detail of a
 806 lawsonite porphyroblast including several garnet crystals, crosscut by thin quartz veins. PPL. (e) Processed
 807 X-ray map of garnet reported in (d), highlighting the inclusion distribution within garnet and its chemical
 808 zoning. (f) Back-scattered (BSE) image of a garnet porphyroblast, showing the distribution of inclusions.
 809 Note the occurrence of a small omphacite inclusion in garnet rim and of a small epidote inclusion in garnet
 810 mantle.
 811

812 **Fig. 6** - Compositional diagrams for the main mineral phases analysed in samples 14-4B and 14-6F/G. (a)
 813 Garnet compositions plotted in the Grs-(Sps+Andr)-(Alm+Prp) diagram. (b) Fe, Mg and Mn X-ray maps of
 814 the same garnet reported in Fig. 3d, e. (c) Omphacite compositions (inclusions in garnet) plotted in the Jd-
 815 Quad-Aeg diagram. (d) Phengite compositions plotted in the Si vs. (Mg + Fe) (a.p.f.u.) diagram. The black
 816 line represents the ideal celadonitic substitution. (e,f) Na-Amphibole compositions plotted in the Si
 817 (a.p.f.u.) vs. Mg/(Mg+Fe⁺²) (e), Si (a.p.f.u.) vs. Na/(Na+Ca) and Si (a.p.f.u.) vs. Fe⁺³/Fe_{tot} (f). (g) Ca-Amphibole
 818 compositions plotted in the Si (a.p.f.u.) vs. Mg/(Mg+Fe⁺²).
 819

820 **Fig. 7** – Metamorphic evolution inferred for samples 14-4B and 14-6F. Sm is the main foliation.
 821

Fig. 8 – (a) P-T pseudosection calculated for sample 14-4B in the MnNCKFMASH model system and at H₂O saturated conditions using the whole rock bulk composition. The variance of the fields varies from two (i.e. 8 phases, white fields) to five (i.e. 5 phases, darker grey fields). Garnet compositional isopleths are reported for garnet core, mantle and rim in dark, medium and light red, respectively (Alm: dashed; Grs: continuous; Prp: dotted; Sps: dashed-dotted lines); phengite compositional isopleths are reported in yellow. The modeled peak assemblage is reported in bold. The black arrow is the prograde portion of the P-T path inferred from the pseudosection. The entire set of garnet compositional isopleths is reported in Fig. SM3. (b, c) Same pseudosection of (a), contoured for lawsonite (b) and garnet (c) modal amount (vol%). Note that lawsonite is predicted to be slightly consumed along the inferred P-T path, whereas garnet is predicted to increase in modal amount.

Fig. 9 – (a) P-T pseudosections calculated for sample 14-6F in the MnNCKFMASH model system and at H₂O saturated conditions using the whole-rock (unfractionated: lower left) and the fractionated (upper right) bulk compositions, respectively, and used to model the growth of garnet core and mantle (unfractionated bulk) and garnet rim (fractionated bulk). The variance of the fields varies from two (i.e. 8 phases, white fields) to four (i.e. 6 phases, darker grey fields). Garnet compositional isopleths are reported for garnet core, mantle and rim in dark, medium and light red, respectively (Alm: dashed; Grs: continuous; Prp: dotted; Sps: dashed-dotted lines); phengite compositional isopleths are reported in yellow. The black arrows are the prograde portions of the P-T path inferred for the growth of garnet core, mantle and rim. The entire set of garnet compositional isopleths is reported in Fig. SM4. (b, c) Same pseudosections of (a), contoured for lawsonite (b) and garnet (c) modal amount (vol%). Note that lawsonite is predicted to be slightly consumed along the inferred P-T path, whereas garnet is predicted to increase in modal amount.

Fig. 10 – (a, b) P-X(Fe₂O₃) and T-X(Fe₂O₃) pseudosections calculated for sample 14-4B in the MnNCKFMASHO model system at T = 420°C and P = 22 kbar, respectively. (c, d) P-X(Fe₂O₃) and T-X(Fe₂O₃) pseudosections calculated for sample 14-6F (fractionated bulk composition) the MnNCKFMASHO model system at T = 470°C and P = 20 kbar, respectively. In all the pseudosections the variance of the fields varies from two (i.e. 8 phases, white fields) to six (i.e. 5 phases, darker grey fields). Garnet compositional isopleths are reported for garnet rim in red (Alm: dashed; Grs: continuous; Prp: dotted; Sps: dashed-dotted lines). The modeled equilibrium assemblages are reported in bold. For both the samples, peak-P conditions decrease with increasing XFe₂O₃ (ΔP = 2-3 kbar for sample 14-4B and ΔP = 1 kbar for sample 14-6F), whereas peak-T conditions do not significantly change at variable XFe₂O₃ values.

Fig. 11 – P/T-X(H₂O) pseudosection calculated for sample 14-4B in the MnNCKFMASH model system along two different P/T gradients: gradient A (a) coincides with the P-T path constrained using the P-T pseudosection calculated with H₂O in excess (black arrow in Fig. 8a); gradient B (b) is steeper (similar to the early prograde P-T evolution of Eastern Himalayan blueschists reported in the literature; Ao and Bhowmik., 2014). The variance of the fields varies from two (i.e. 7 phases, white fields) to five (i.e. 5 phases, darker grey fields). Garnet compositional isopleths are reported for garnet core and rim in dark and light red, respectively (Alm: dashed; Grs: continuous; Prp: dotted; Sps: dashed-dotted lines). The observed equilibrium assemblage is reported in bold. The white dotted lines in both pseudosections represent the H₂O-saturation surface and divide the pseudosections in a H₂O-saturated part on the right and in a H₂O-undersaturated part on the left. The intersection of garnet compositional isopleths on the H₂O-saturation surface in (a) confirms that garnet growth (with the measured composition) occurred at H₂O-saturated conditions; garnet core compositional isopleths do not intersect in (b), thus implying that gradient B is not compatible with the observed mineral assemblage and compositions.

868

869 **Fig. 12** – (a,b) P/T-X(H₂O) pseudosections calculated for sample 14-6F in the MnNKCFMASHO model system
870 along the same gradient A as in Fig. 11a and using the whole-rock (unfractionated: a) and the fractionated
871 (b) bulk compositions. The variance of the fields varies from two (i.e. 7 phases, white fields) to five (i.e. 5
872 phases, darker grey fields). Garnet compositional isopleths are reported for garnet core and rim in dark and
873 light red, respectively (Alm: dashed; Grs: continuous; Prp: dotted; Sps: dashed-dotted lines). The white
874 dotted line represents the H₂O-saturation surface and divides the pseudosections in a H₂O-saturated part
875 on the right and in a H₂O-undersaturated part on the left. The intersection of garnet compositional
876 isopleths on the H₂O-saturation surface confirms that garnet growth (with the measured composition)
877 occurred at H₂O-saturated conditions. (c-f) Same P/T-X(H₂O) pseudosection of (a, b) contoured for lawsonite
878 (c, d) and garnet (e, f) modal amounts (in vol%). The red ellipses indicate the P-T-X(H₂O) conditions inferred
879 for the growth of garnet core and rim from Fig. 12a, 12b. H₂O addition is required to form lawsonite (c, d).
880 A protracted H₂O influx at high pressure is required in order to allow the contemporaneous growth of
881 garnet, which requires H₂O-saturated conditions (e, f) and lawsonite, whose growth subtracts H₂O to the
882 system (c, d) (see text for further details).

883

884 **Fig. 13** - (a) P-T path constrained for the Sapi-Shergol blueschist unit (red thick vs. dotted arrows are the P-T
885 paths constrained in the MnNKCFMASHO vs. MnNKCFMASH system, respectively; the P-T path previously
886 constrained by Honegger et al., 1989 and Guillot et al., 2008 is reported in orange) compared with the P-T
887 paths of the other Himalayan blueschist rocks: Shangla (in yellow: Guillot et al., 2008) and Nagaland
888 Ophiolite Complex (in green: Ao and Bhowmik, 2014). The dashed grey arrow is the schematic P-T path
889 followed by the sedimentary particles in the accretionary wedge, as resulting from the thermomechanical
890 numerical study of Yamato et al. (2007). (b) P-T diagram comparing the maximum P-T conditions for well-
891 documented examples of accretionary terranes in subduction zones (modified from Agard and Vitale
892 Brovarone, 2013 and Plunder et al., 2015, with references therein) with the P-T conditions experienced by
893 the Sapi-Shergol blueschist unit (this study; red squares) and the Nagaland Ophiolite Complex of far-eastern
894 Himalaya (Ao and Bhowmik, 2014; green square). Data are mainly derived from: Agard et al. (2001b),
895 Plunder et al. (2012): Western Alps; Ravna et al. (2010), Vitale Brovarone et al. (2011, 2013), Agard and
896 Vitale Brovarone (2013): Corsica; David and Whitney (2008), Plunder et al. (2015): Turkey; Warren et al.
897 (2005), Warren and Waters (2006), Agard and Vitale Brovarone, (2013): Oman; Agard et al. (2006): Zagros;
898 Fitzherbert et al. (2003, 2004, 2005), Agard and Vitale Brovarone (2013), Vitale Brovarone and Agard
899 (2013): New Caledonia; Banno et al. (2000), Page et al. (2006), Tsujimori et al. (2006), Ernst and McLaughlin
900 (2012), Ukar and Cloos (2014): Franciscan Complex (western USA).

Fig. 1

[Click here to download high resolution image](#)

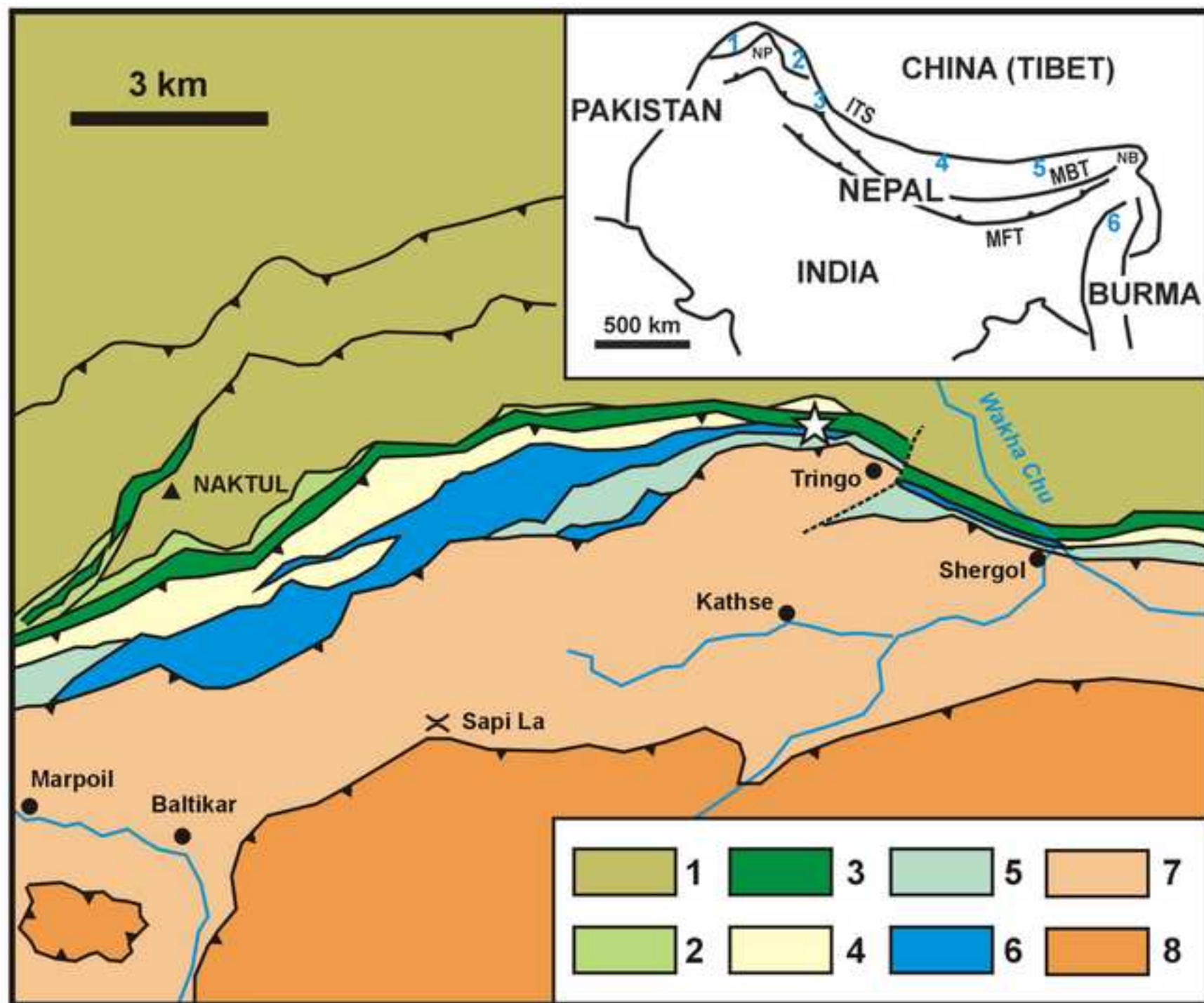


Fig. 2

[Click here to download high resolution image](#)

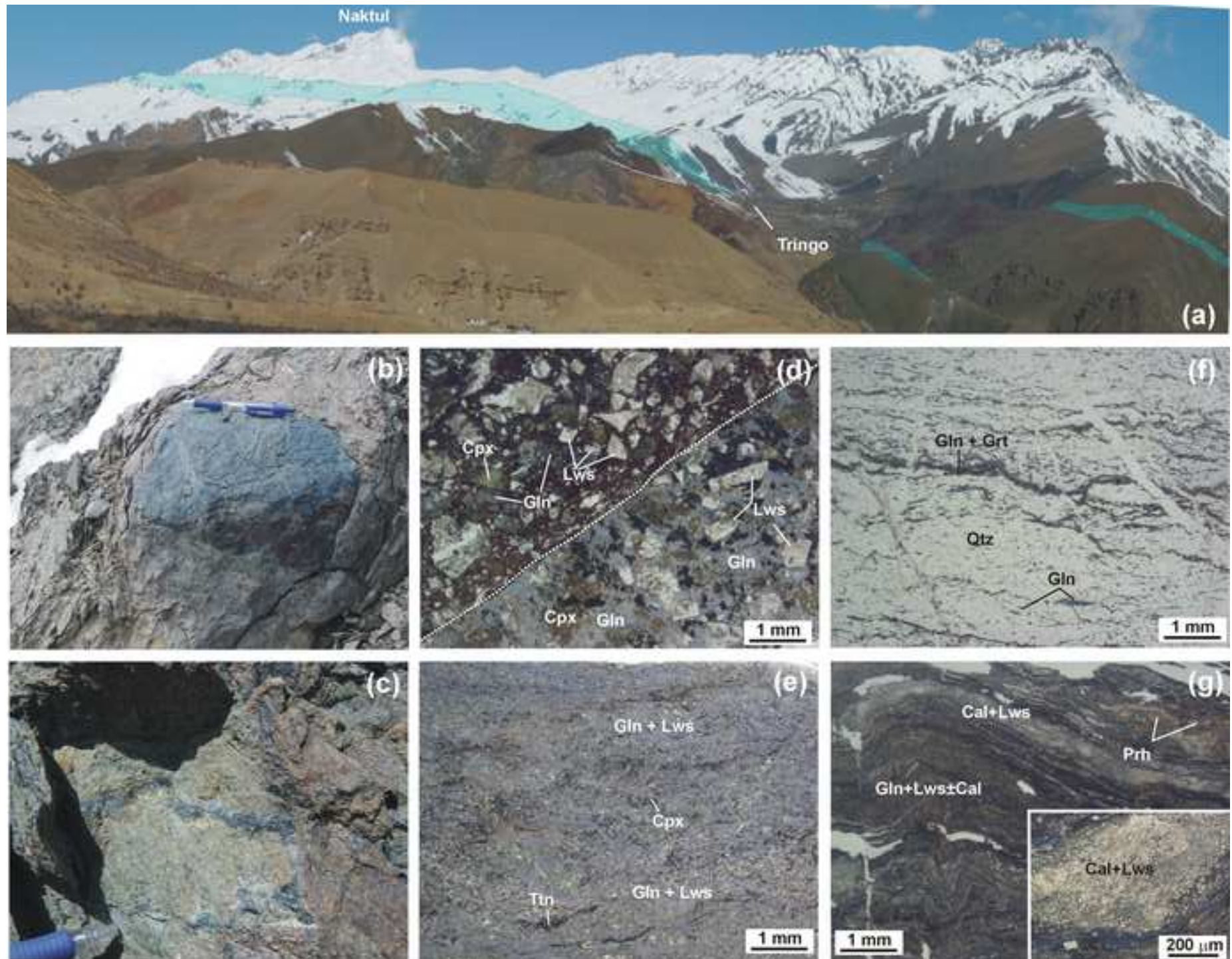
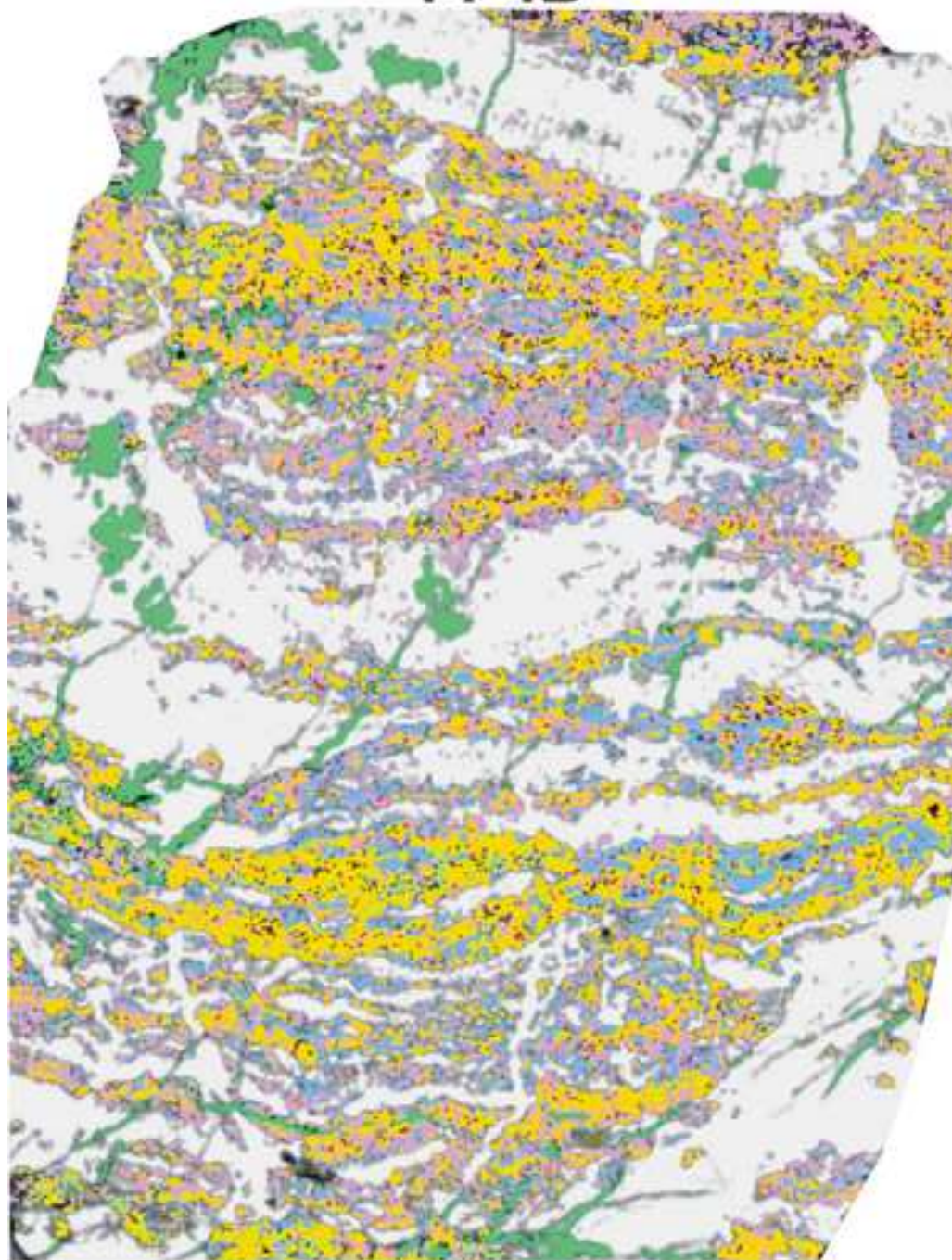


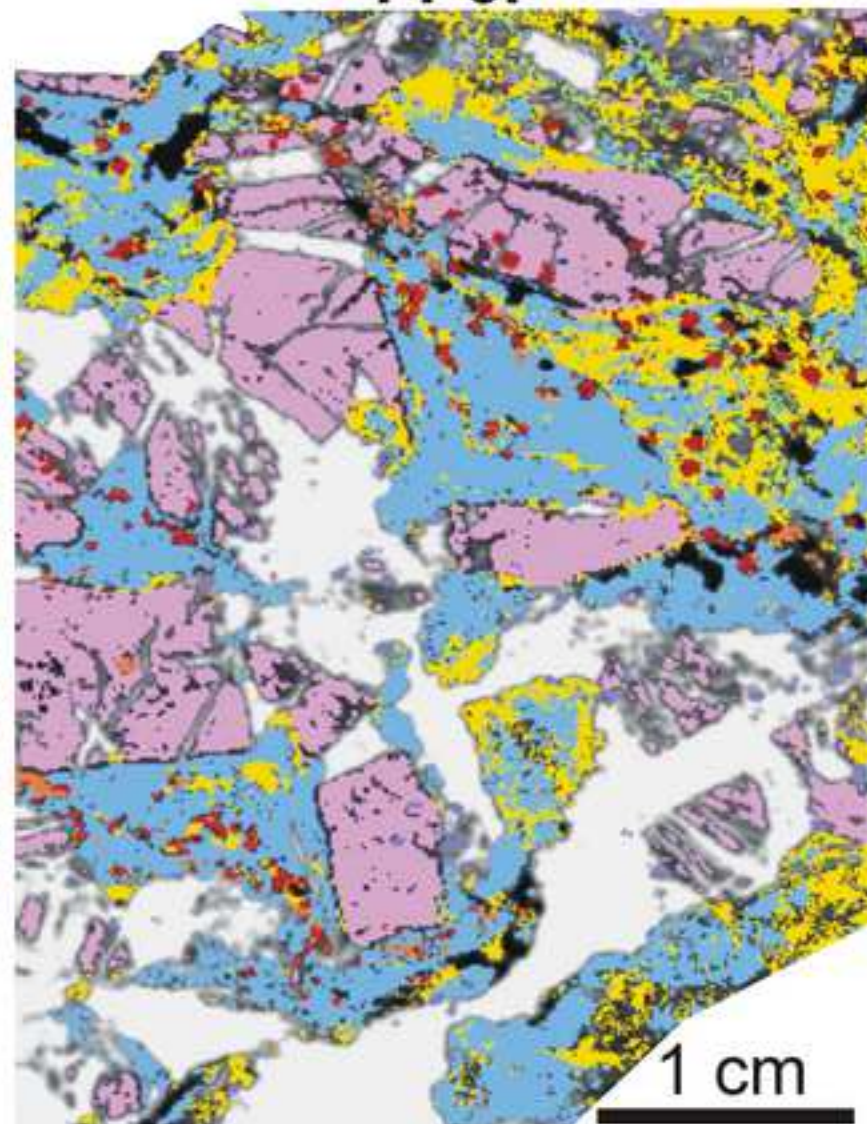
Fig. 3

[Click here to download high resolution image](#)

14-4B



14-6F



Qtz	Lws	Gln	Phe	Ttn
Grt _C	Grt _R	Cal	Ab	Ap

Fig. 4

[Click here to download high resolution image](#)

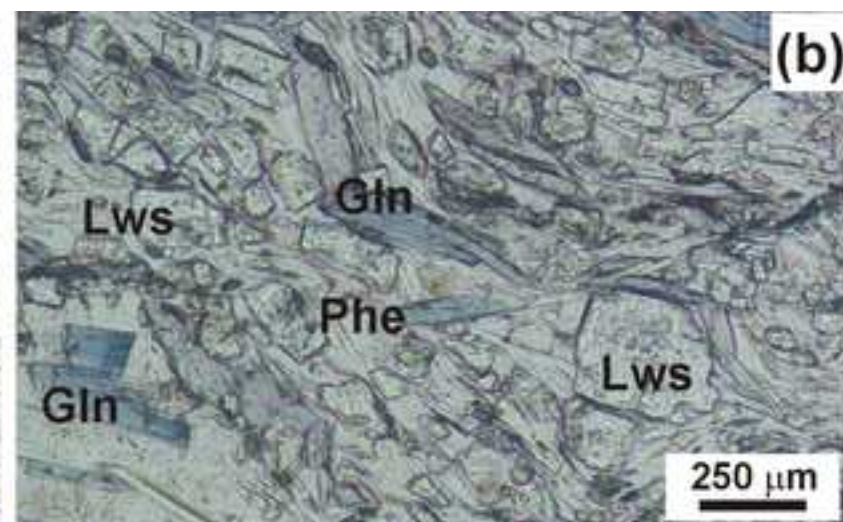
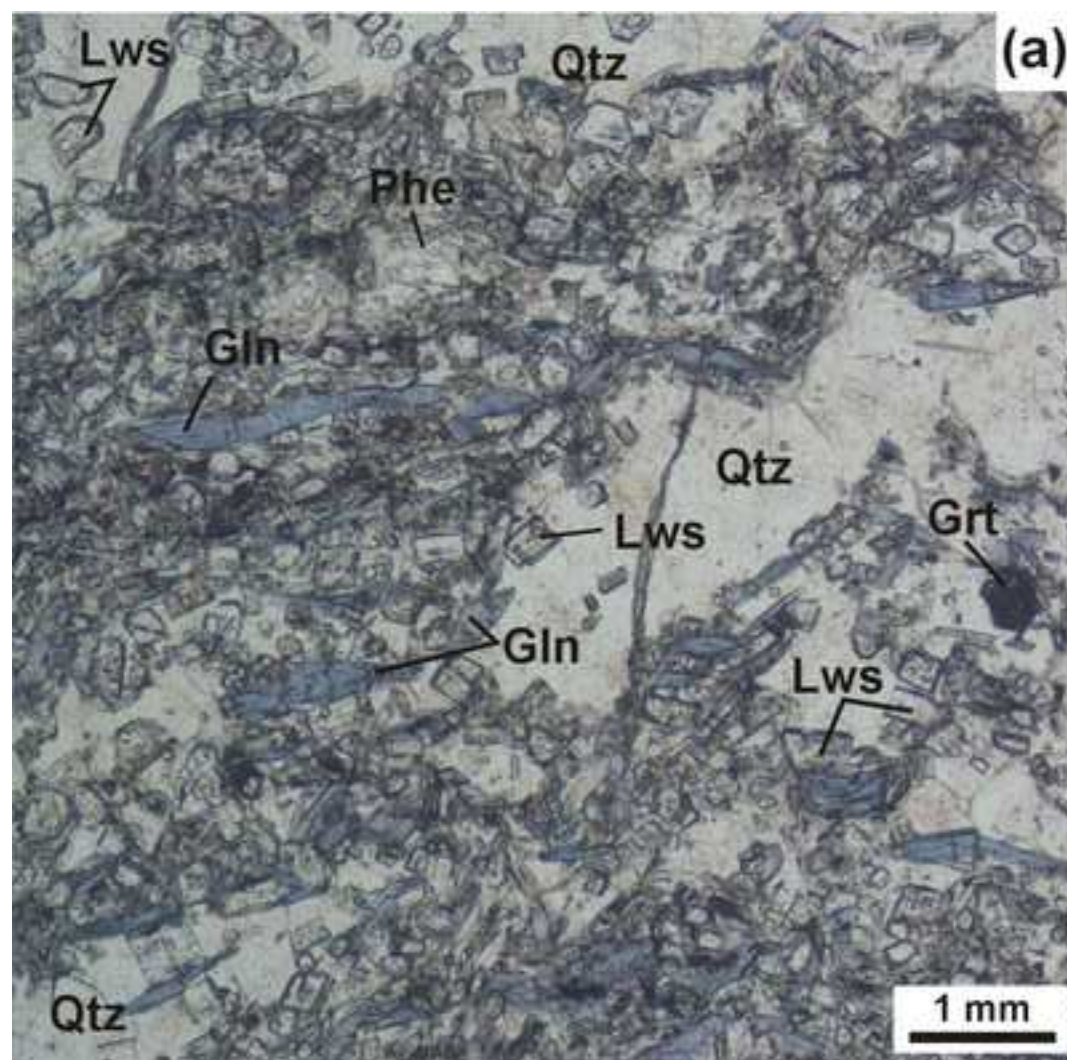


Fig. 5
[Click here to download high resolution image](#)

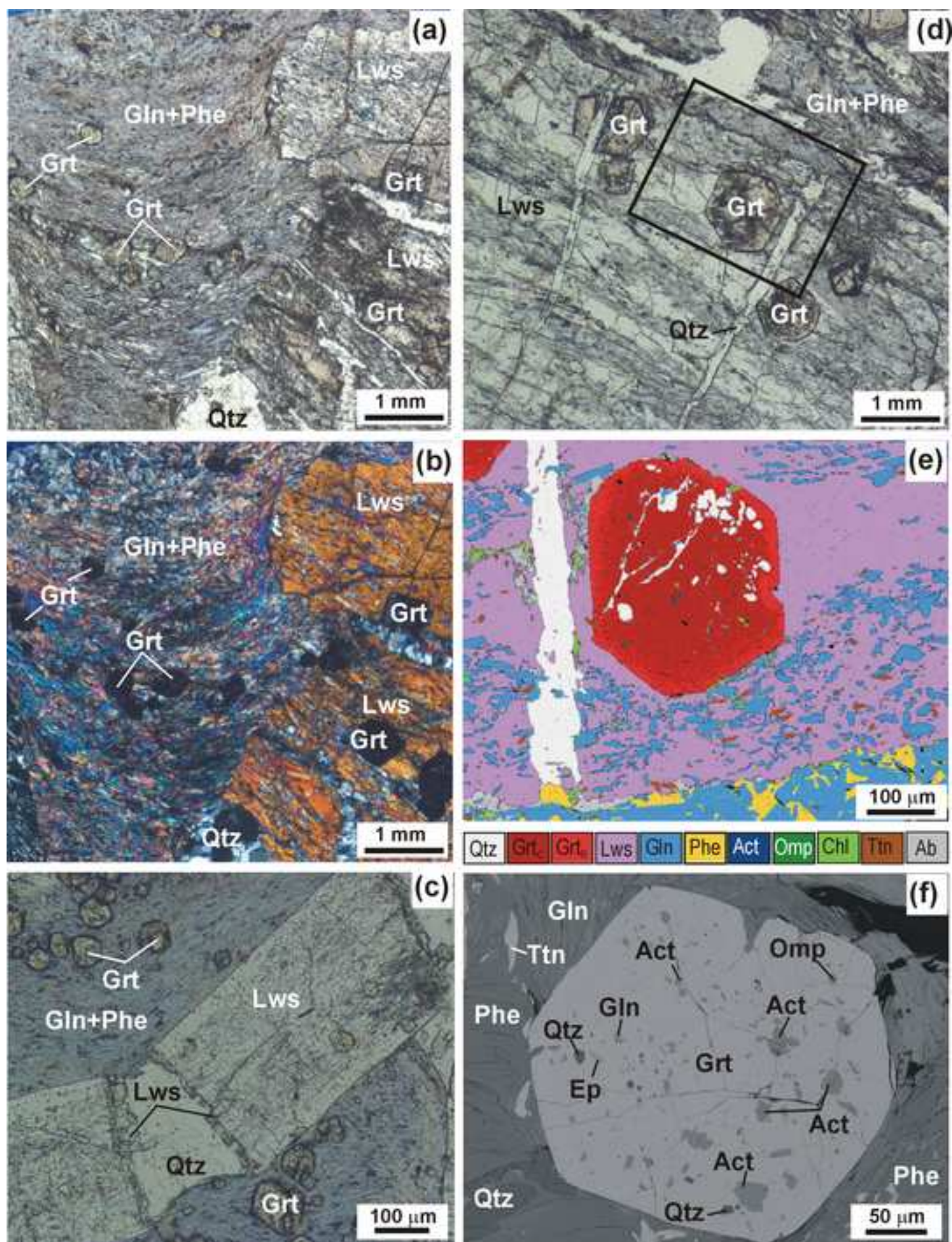


Fig. 6
[Click here to download high resolution image](#)

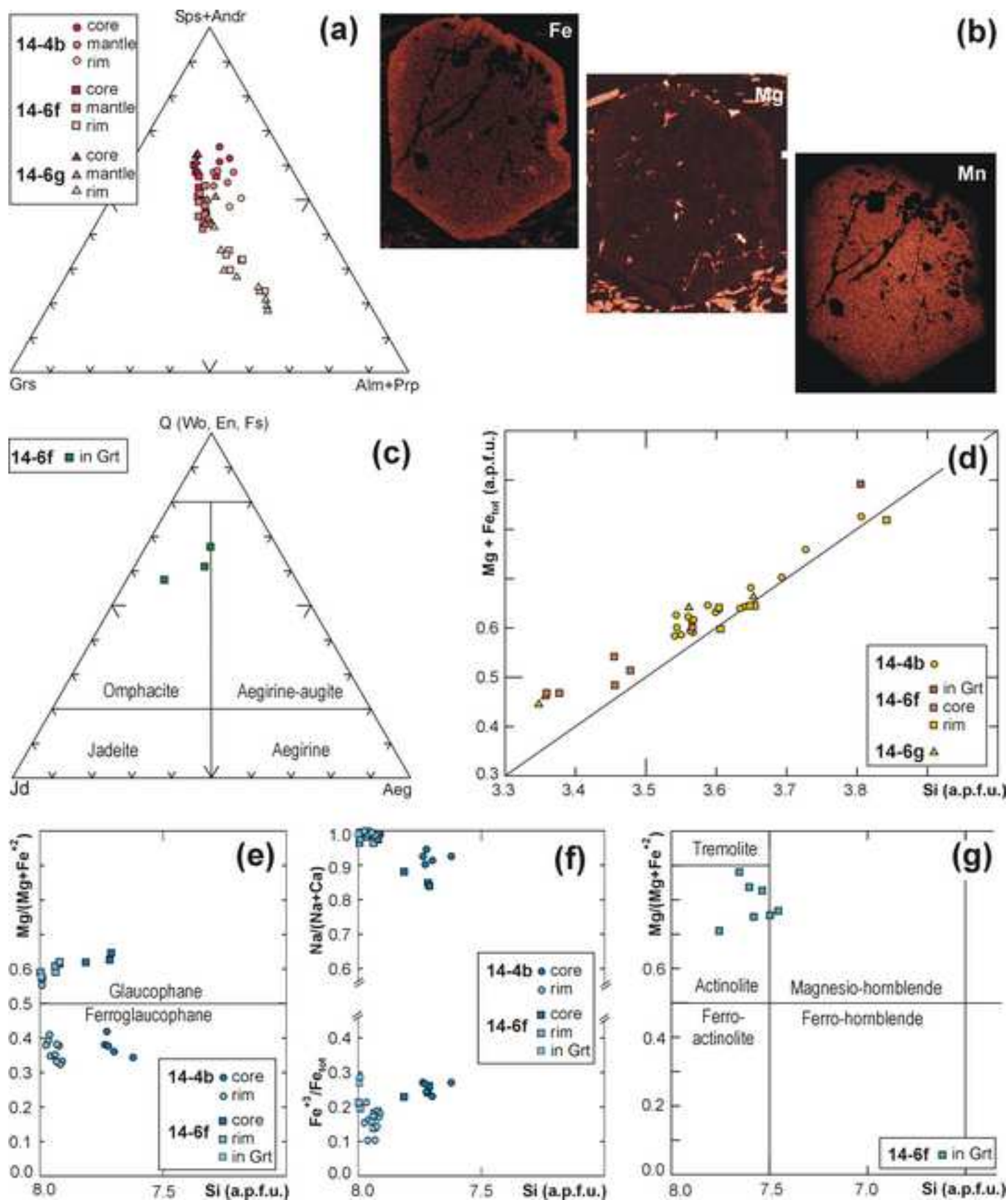
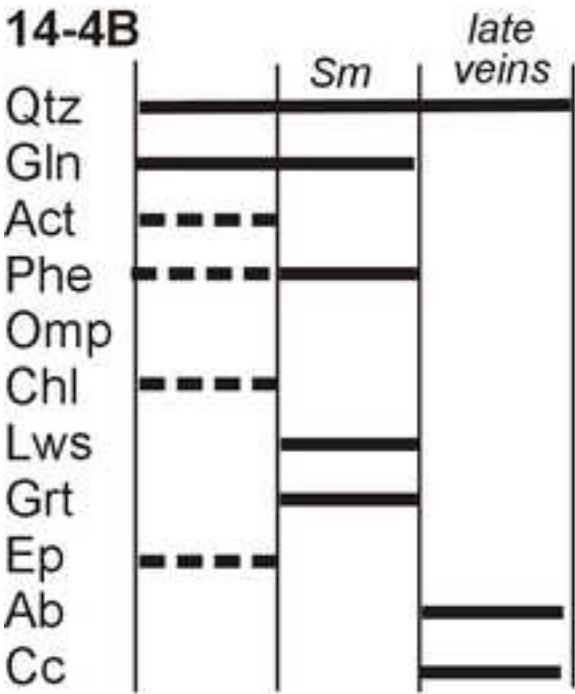


Fig. 7
[Click here to download high resolution image](#)

14-4B



14-6F

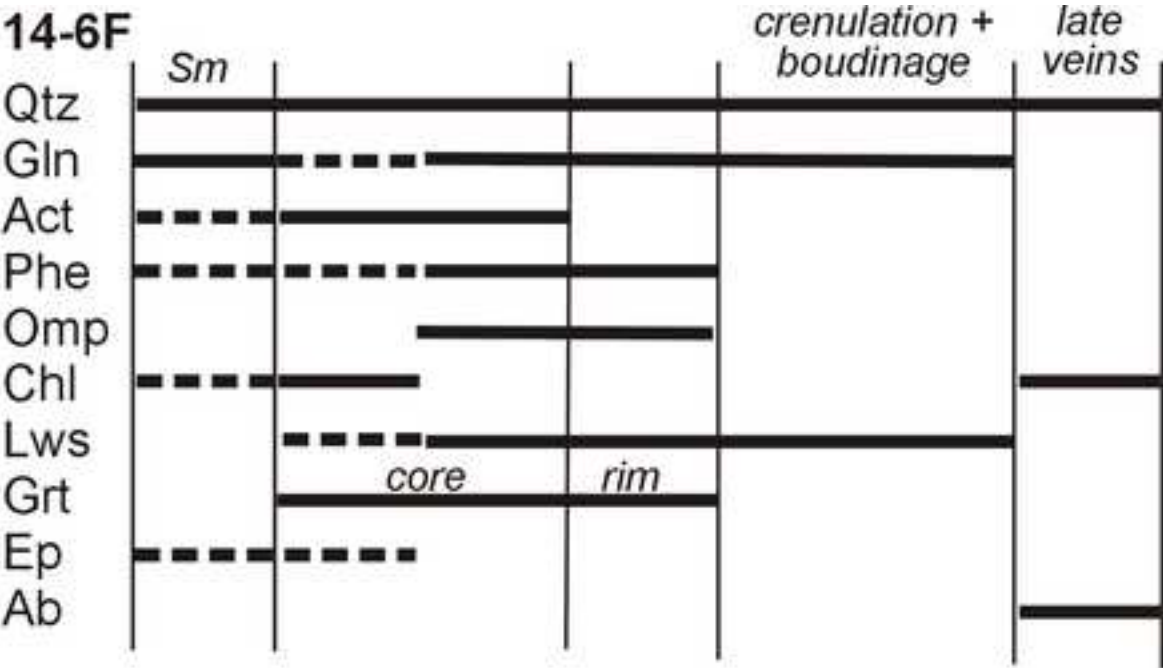


Fig. 8

[Click here to download high resolution image](#)

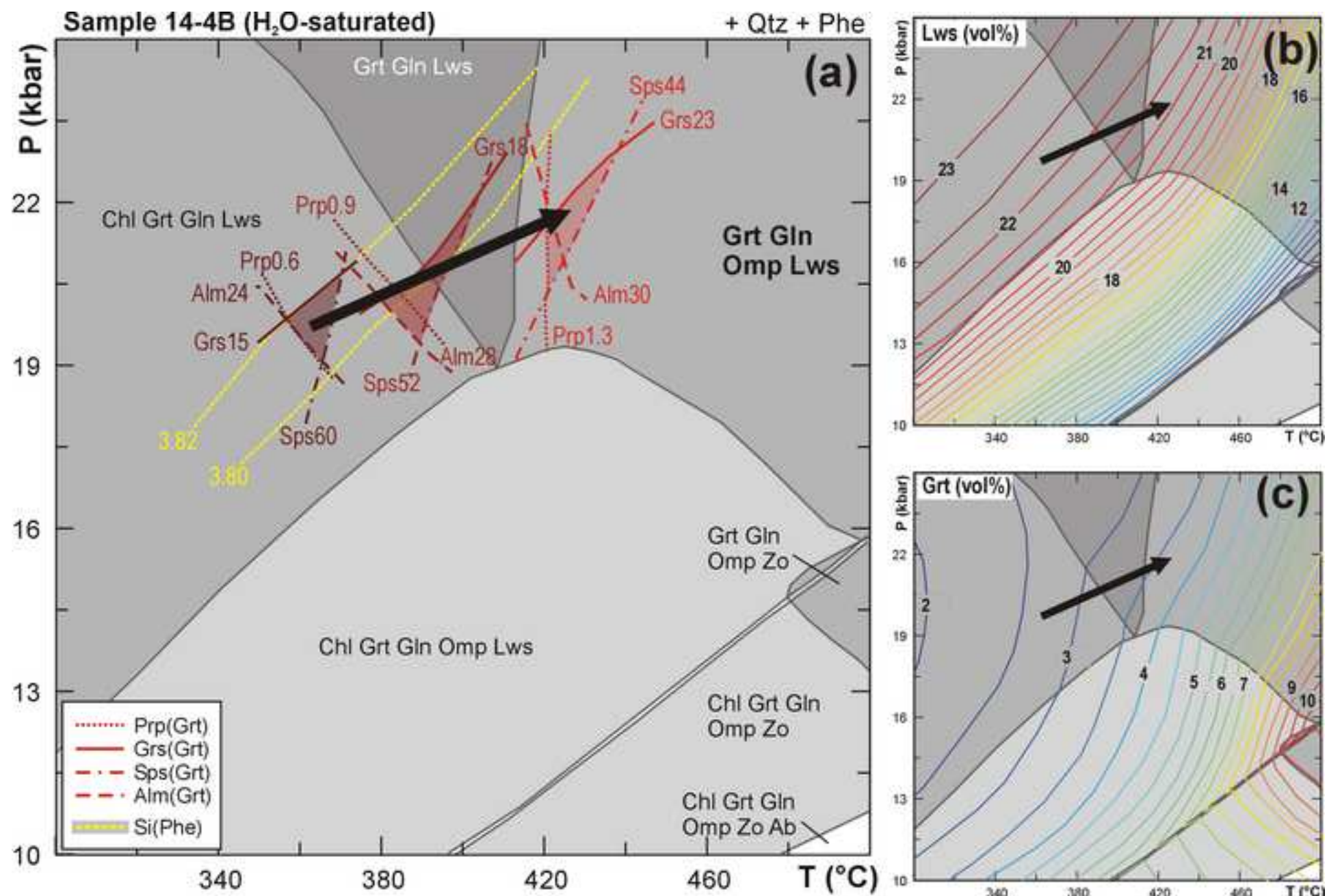


Fig. 9

[Click here to download high resolution image](#)

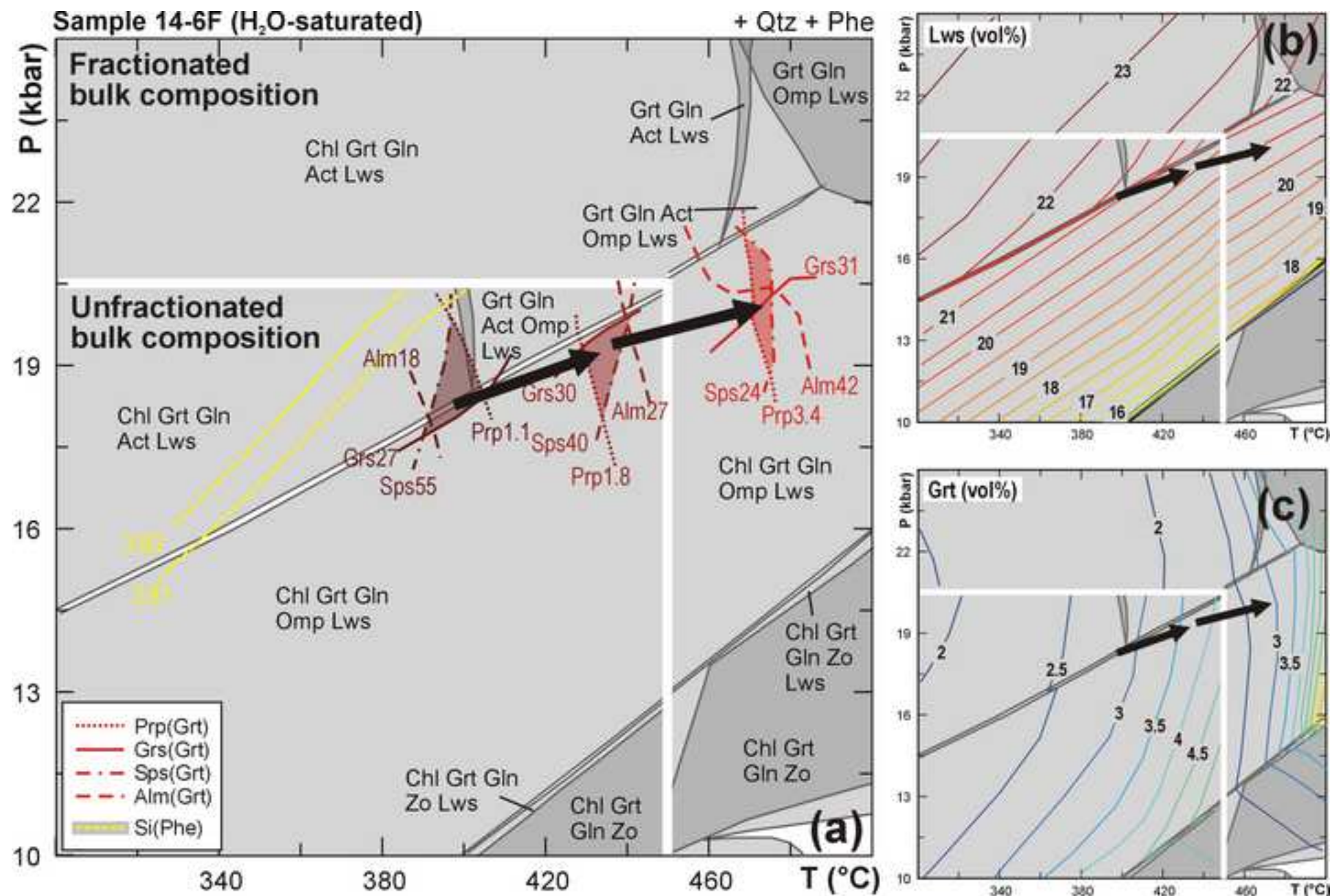


Fig. 10
[Click here to download high resolution image](#)

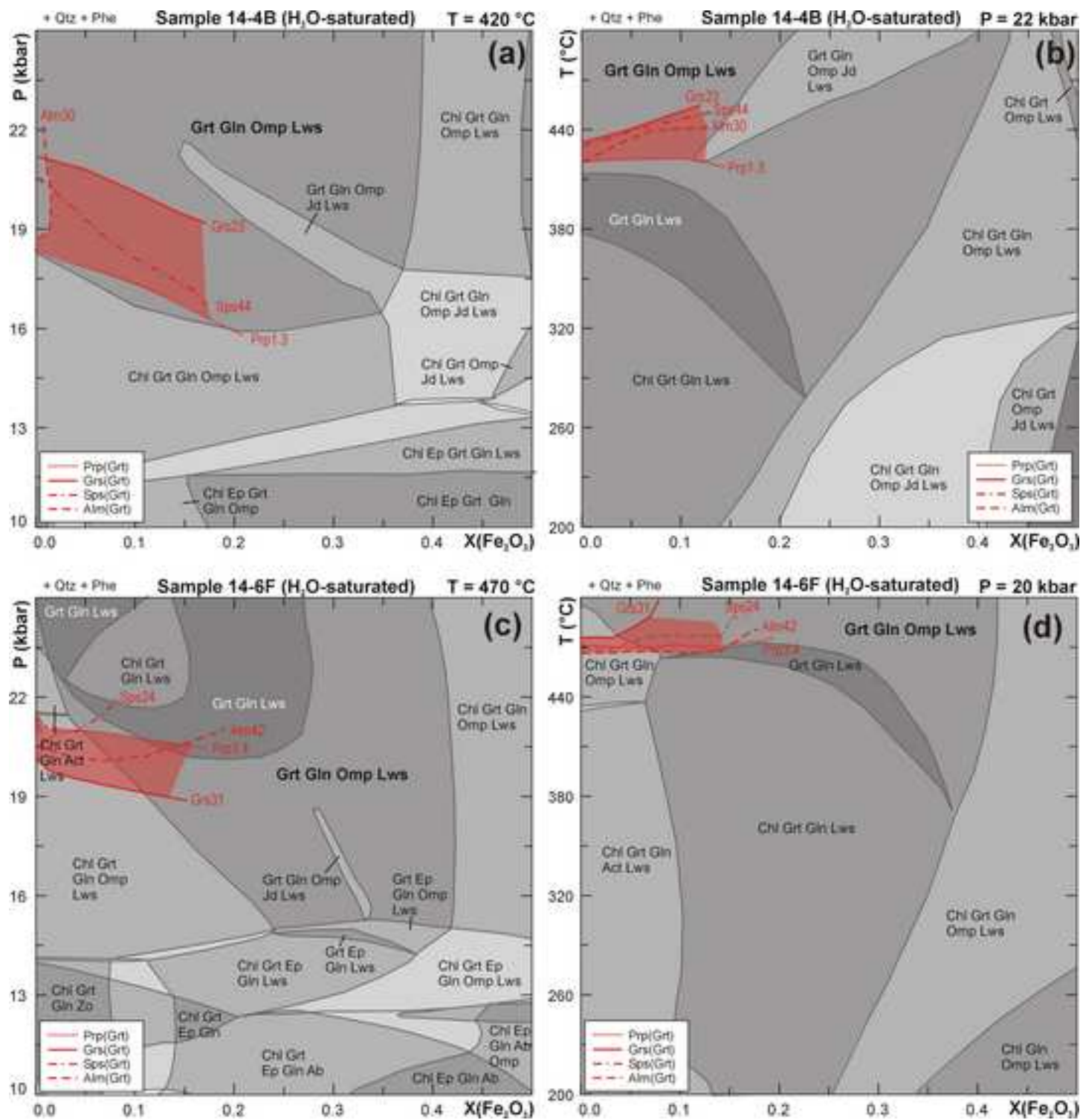


Fig. 11

[Click here to download high resolution image](#)

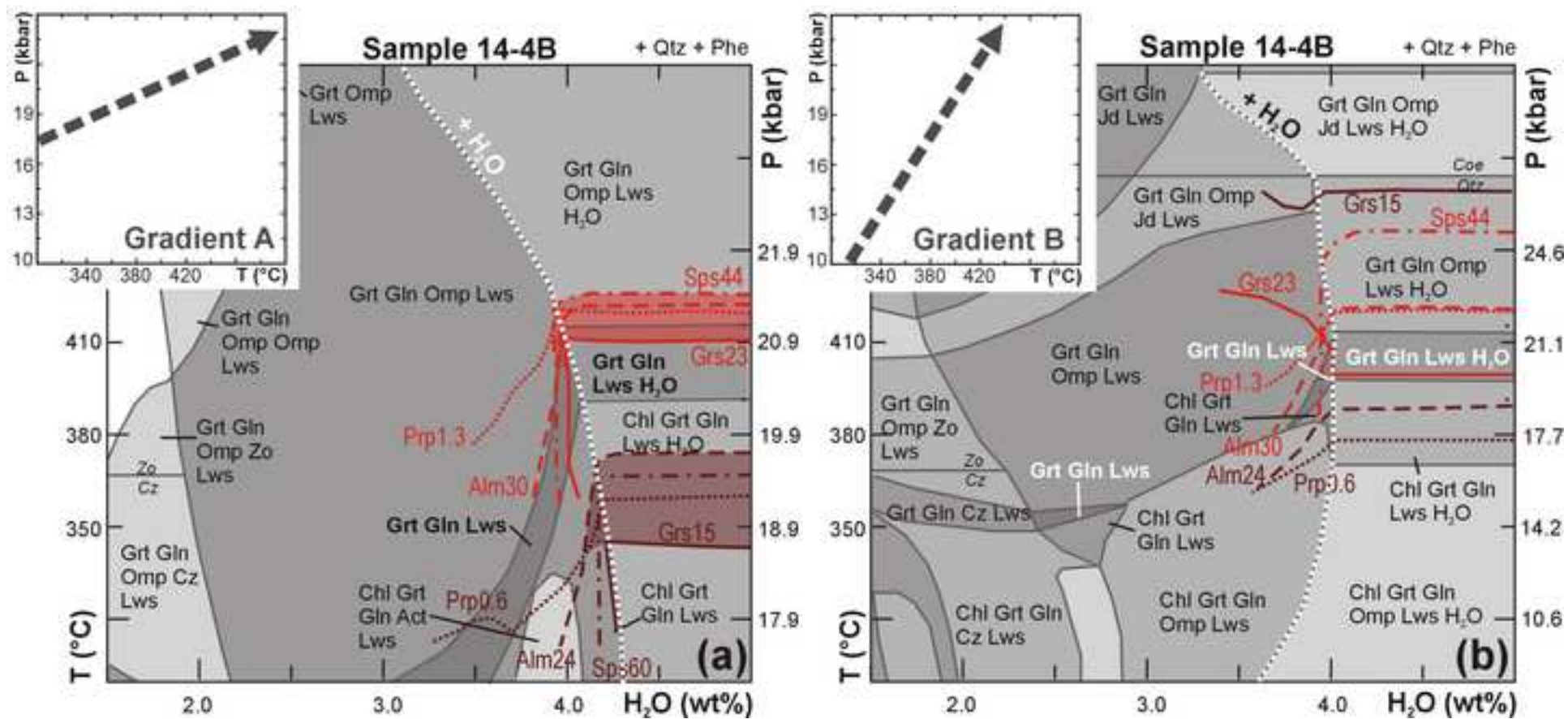


Fig. 12
[Click here to download high resolution image](#)

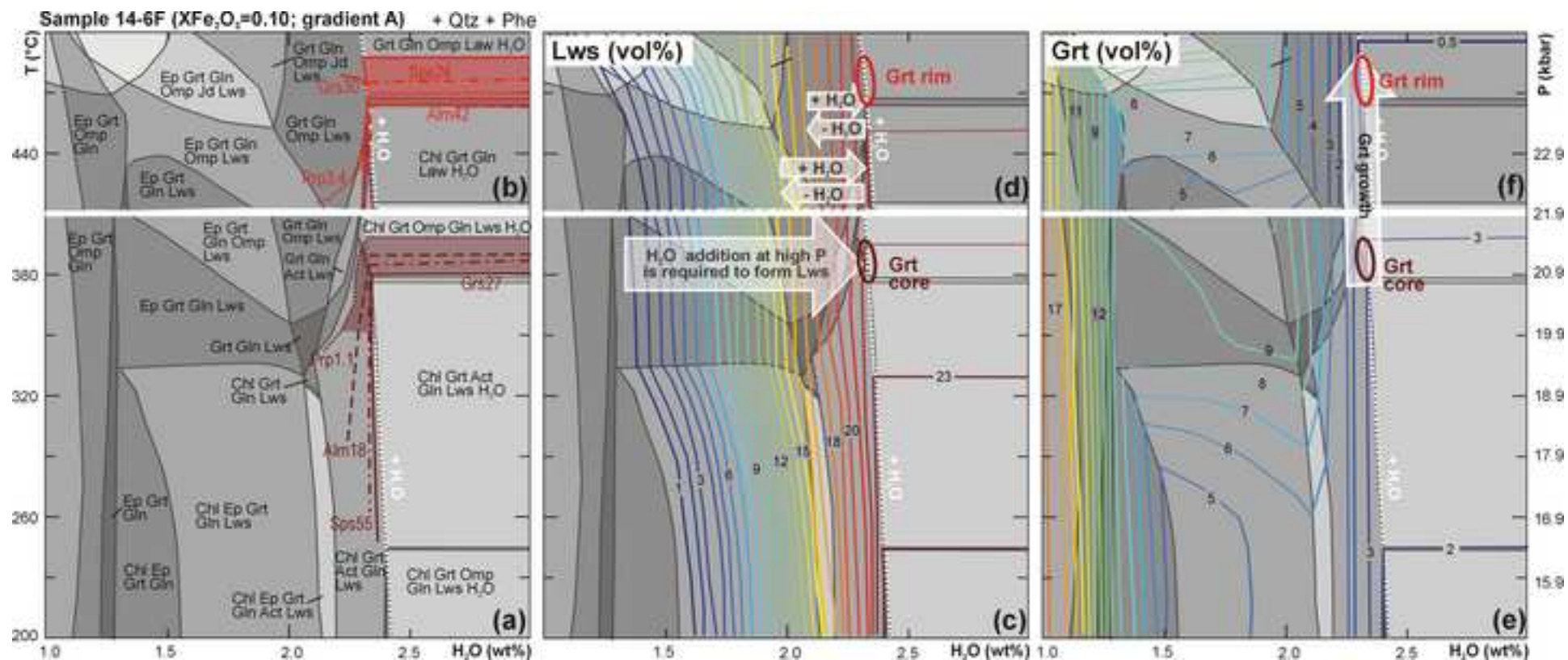


Fig. 13
[Click here to download high resolution image](#)

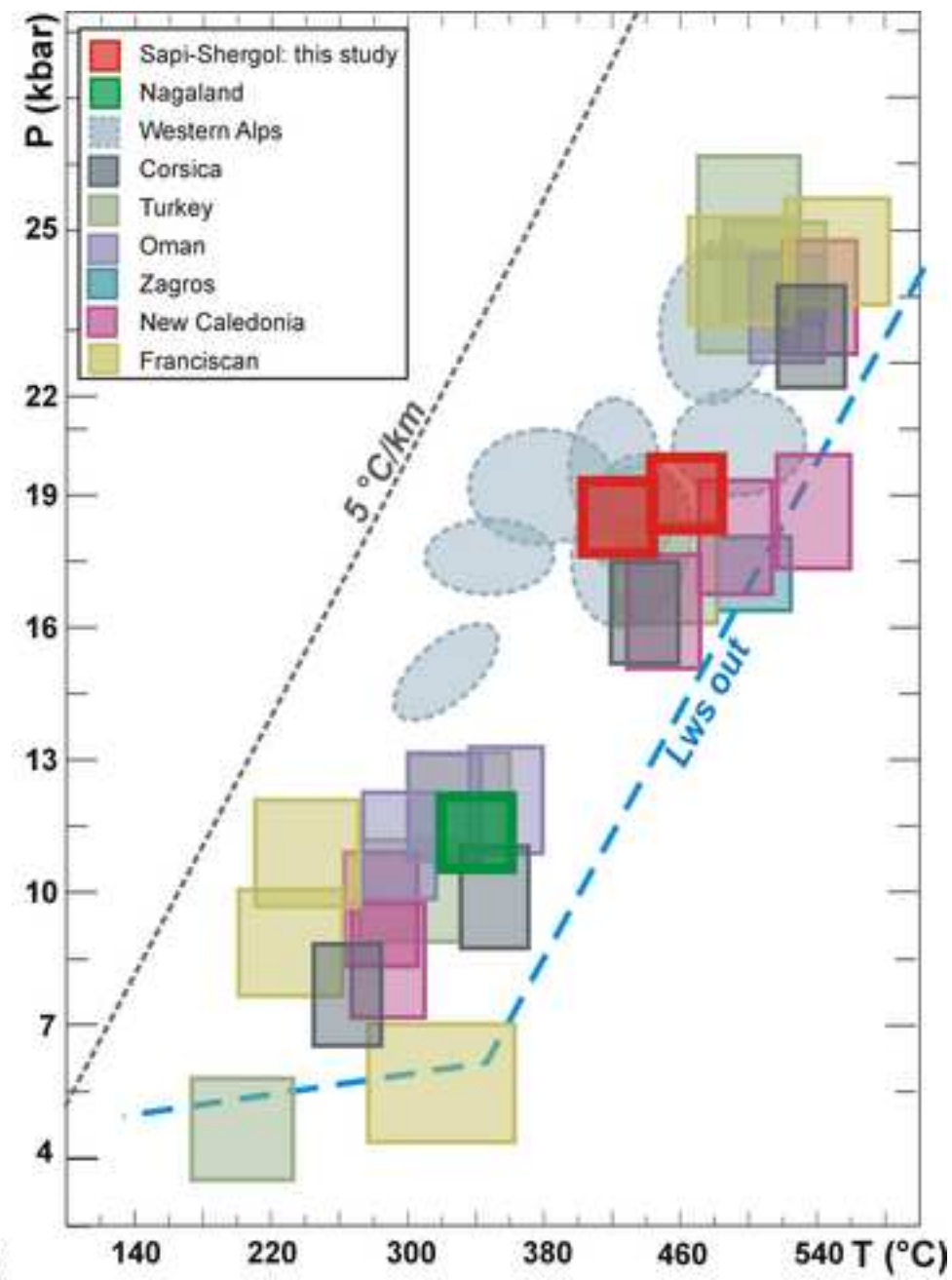
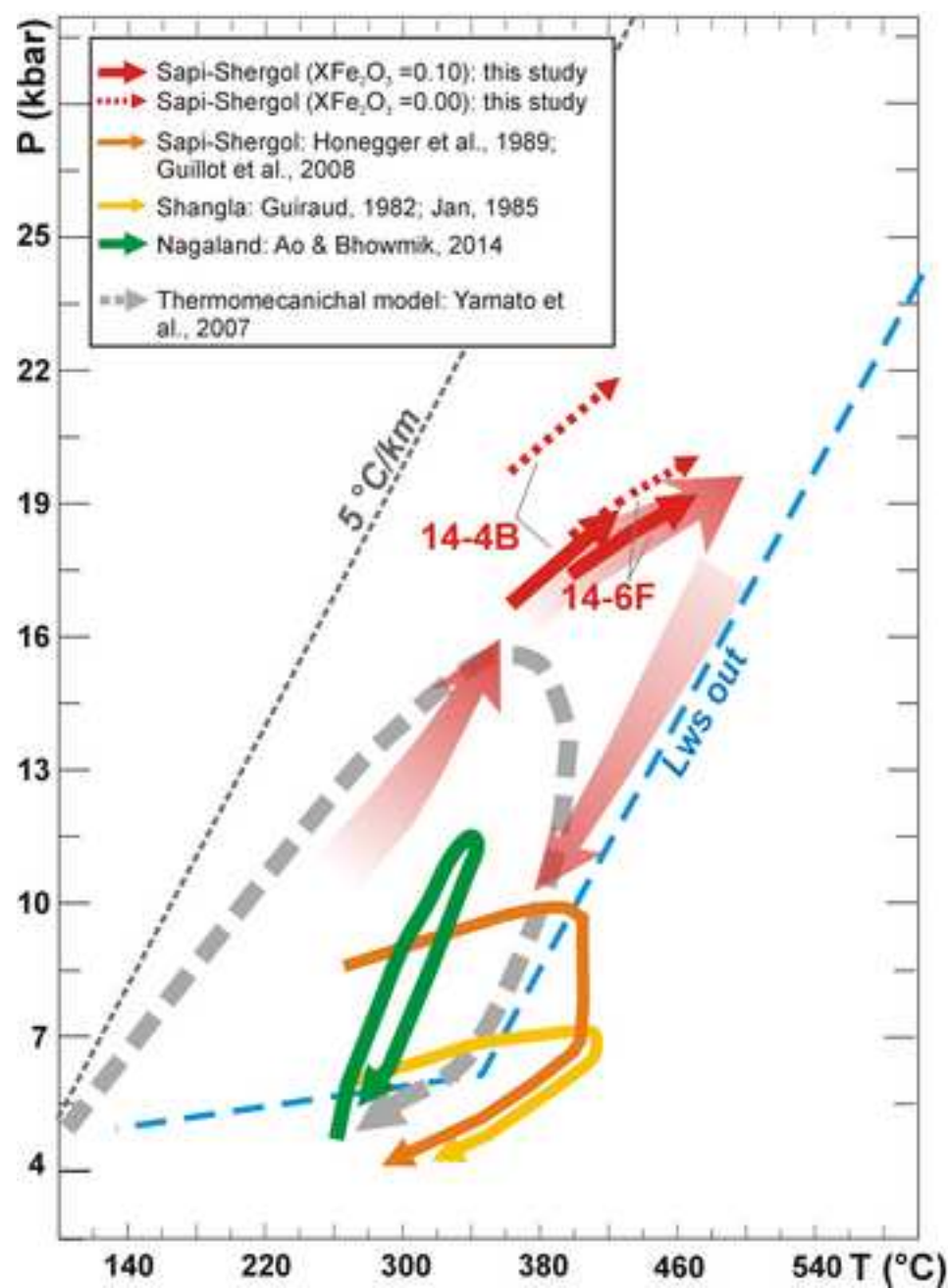


Table 1 - Modal (vol%) and bulk (wt%) compositions of samples 14-4B and 14-6F

Sample	14-4B	14-6F	
Qtz	42	21	
Lws	21	22	
Phe	22	9	
Gln	12	44	
Grt	3	4	
Total	100	100	

Sample	14-4B	14-6F	
		unfractionated	fractionated
SiO ₂	70.26	61.69	62.91
Al ₂ O ₃	14.40	15.76	15.48
FeO	4.20	7.14	7.01
MgO	1.80	4.75	4.96
MnO	1.05	0.93	0.06
CaO	4.66	5.32	4.95
Na ₂ O	0.96	3.34	3.51
K ₂ O	2.67	1.07	1.12
Total	100.00	100.00	100.00